Modelling of the retention dynamics at the transition from High-confinement phase to Low-confinement phase in a full-tungsten tokamak

Julien Denis, Yves Ferro, Jérôme Bucalossi, Guido Ciraolo, Etienne A Hodille, Bernard Pegourié, Hugo Bufferand, Christian Grisolia, Thierry Loarer, Eric Serre, et al.

Modelling of the retention dynamics at the transition from High-confinement phase to Low-confinement phase in a full-tungsten tokamak.

J. Denis[a,b], Y. Ferro[a], J. Bucalossi[b], G. Ciraolo[b], E. A. Hodille[b], B. Pégourié[b], H. Bufferand[b], C. Grisolia[b], T. Loarer[b], E. Serre[c], S. Vartanian[b], Y. Marandet[a], and JET Contributors*

[a] *Aix Marseille Univ, CNRS, PIIM, Marseille, France.*
[b] *CEA, IRFM, F-13108 Saint-Paul-lez-Durance, France.*
[c] *Aix Marseille Univ, CNRS, Centrale Marseille, M2P2, Marseille, France.*

e-mail address: julien.denis@univ-amu.fr

Abstract

The dynamic retention of deuterium in a full-tungsten JET-like tokamak is investigated thanks to the Dynamics of Wall Elements (DWE) code. DWE is a wall model coupled to the SolEdge-EIRENE edge-plasma transport code. It is composed of two internal codes: *(i)* WE-temp, which determines the wall temperature, and *(ii)* MHIMS, which determines the transport, trapping and desorption of hydrogen isotopes in the wall material. In this work, four consecutive discharges are modeled and analysed with DWE. These discharges are identical and present a transition from a H-mode phase to a L-mode phase, which induces strongly different plasma-wall interactions. The main results are as follows. *(i)* A release of deuterium is observed at the vicinity of both strike-points at the end of the H-mode phase. This dynamics is explained by an increase of the wall temperature at both strike-points due to the strong plasma heat flux received there, leading to detrapping from trap with low detrapping energy. On the contrary, during the subsequent L-mode phase, the wall temperature at the strike-points decreases, leading to retention by filling the trap emptied during the H-mode. *(ii)* A release of deuterium from the first-wall is unexpectedly observed at the transition between the H-mode and the L-mode. This release is a consequence of a decrease in implantation energy between the two phases, as it entails a shallower implantation of deuterium. Despite the different material considered in the simulation, the latter result offers a possible explanation of the strong transient release of deuterium experimentally observed in the JET-ILW at the NBI cut-off during high density H-mode discharges.

1 Introduction.

The study of Hydrogen Isotopes (HI) retention in the wall of nuclear fusion reactors has attracted lots of attention over the past few decades, mainly due to the safety issue related to the long-term retention of radioactive tritium [1]. The tritium worldwide stock is also limited and its loss in the wall will have to be limited during the operation of the ITER fusion device. Another aspect of retention is the so-called *short-term/dynamic retention*, i.e. the fuel uptake in the wall during discharge and its release in the vacuum vessel, mostly between discharges, but also during the discharge itself. Although

*See the author list of "Overview of JET results for optimising ITER operation" by J. Mailloux et al 2022 Nucl. Fusion 62 042026

it is harmless in terms of safety, as the released HI are retrieved by the reactor pumping system, the dynamic retention can directly impact the discharge control. It can have a positive effect during the discharge start-up phase as the wall acts as a pump, allowing a better control of the plasma density [2]. On the other hand, it can represent a real risk for the discharge control, as the quantity of HI stored in the wall is much higher than the one in the plasma. As an example, in the JET ITER-Like Wall (JET-ILW) tokamak, composed of a tungsten (W) divertor and a beryllium (Be) first-wall, the quantity of HI dynamically retained in the wall is 4 to 24 times higher than the quantity of HI ions in the plasma depending on the plasma scenarios [2]. A release of this retained particles into the plasma can induce an uncontrolled increase of the plasma density if it is not removed by the pumping system, which can ultimately lead to the abrupt termination of the discharge. This loss of density control has already been observed during long plasma operation in present tokamaks with inertially-cooled Plasma Facing Components (PFCs). In the Tore-Supra tokamak with Multilimiter Configuration made of carbon (C), a slow and continuous rise of the density has been detected during such operation, which entailed a disruption of the discharges [3]. The higher the input power, the faster the density raised and the quicker the disruption occurred. This loss of density control was attributed to the outgassing of water from inertially cooled PFCs located in remote areas of the vacuum vessel which were heated by the radiated power from the plasma. In the JT-60U tokamak made of a C wall, a transient release of particle from the outer divertor plate heated by the plasma was observed during long and high-power-heated discharges [4], leading to the creation of a high radiative area called MARFE close to the X-point. A similar discharge was conducted at higher initial wall temperature, leading to an earlier release of particle and to an earlier MARFE formation, resulting in a disruption of the discharge. Such phenomenon has not been observed in JET-ILW due to the short duration of the discharges (< 30 s). Still a large dynamic retention is observed during high density H-mode discharges, since up to 10^{23} deuterium (D) atoms are retained in the wall (a factor of 24 higher than the plasma D ion content) [2]. 70% of this quantity is already released during the discharge, at the transition between the H-mode phase and the L-mode phase when Neutral Beam Injection (NBI) heating is switched-off. A slight increase of the plasma density is also observed at the same time, without impact on the discharge itself. This transient release of particles cannot be attributed to material heating as the input power decreases between these two phases.

The experimental study of these dynamic retention is challenging. Only gas balance analysis provides global retention quantities [2, 4, 5]. However, it is known that these dynamics are local, with some areas of the wall which pump particle while others release particles to the plasma [4]. This local retention behaviour could be assessed via numerical modelling tools. Among them, the SolEdge-EIRENE edge-plasma transport code [6] has the ability to simulate plasma-wall interaction up to the wall with complex geometry, assuming a wall toroidal symmetry. It can provide the local implantation quantities for both ions and atoms all along the wall, allowing the modelling of retention dynamics at the scale of nuclear fusion devices. An extension of this code, called Dynamics of Wall Elements (DWE), was developed for that purpose. DWE uses the SolEdge-EIRENE outputs to simulate HI implantation, transport and retention in the materials composing the vacuum vessel. DWE was previously used to model a sequence of four similar discharges in the JET tokamak [7]. Due to the incompleteness of the available models to describe the HI-Be interaction, a full-W wall model was used to perform these simulations. Nonetheless, the analysis of the results revealed that DWE was able to qualitatively reproduce experimental trends observed in the JET-ILW [7], i.e. *(i)* the decay of the retention flux experimentally observed during plasma discharge (a retention flux on the order of 10^{21} D.s^{-1} which decays within several seconds [2]), and *(ii)* the pressure drop measured between discharge (with a $t^{-0.74}$ trend in the simulation DWE, a $t^{-0.89}$ in the experiment). However, the quantity of desorbed D between discharges (and therefore the dynamic retention reservoir) was clearly underestimated in the simulation. The differences in terms of amplitude and dynamics with the experiment were attributed to the consideration of a full-W wall, as Be is known to store a higher amount of HI in the implantation zone than W [8, 9] and to desorb HI at lower material temperature [10, 11, 12].

The present paper specifically focuses on the retention dynamics during discharges obtained from the same simulation as in reference [7]. The discharge of interest presents two stationary phases, an initial

H-mode phase followed by a L-mode phase, leading to different implantation conditions. The next section focuses on the experimental JET plasma discharge used as baseline scenario for the modelling presented in this article. In section 3, the modelling of both stationary phases of the discharge with the SolEdge-EIRENE code is presented and the variation of the implantation quantities is studied. The DWE code is presented in section 4 while section 5 is dedicated to the simulation of dynamic retention during the four consecutive discharges with DWE. This simulation exemplifies retention dynamics during the H-mode to L-mode transition, which are explained in section 6 via an analytical model. The article ends with a discussion about a possible explanation of the retention dynamics experimentally observed in JET-ILW [2] and in JT-60U [4].

2 Experimental plasma discharge.

In order to simulate relevant discharges with a H-mode to L-mode transition, we based our modelling on a real device discharge, i.e. the JET pulse number 89044 (#JPN89044, pure D plasma, $B_t = 2.4$ T, $I_p = 2$ MA), which was performed during the JET-ILW 3 campaign (2015-2016). The time evolution of the discharge parameters are plotted in figure 1. The plasma is run in diverted configuration with inner and outer strike-points located on the top of vertical tile 3 and on the horizontal tile 5 Stack C respectively (cf. figure 2). This configuration is maintained during 24.9 s while the total pulse duration is 26.9 s. This indicates that the two inner limiter phases (at the beginning and at the end of the pulse) have a negligible time duration.

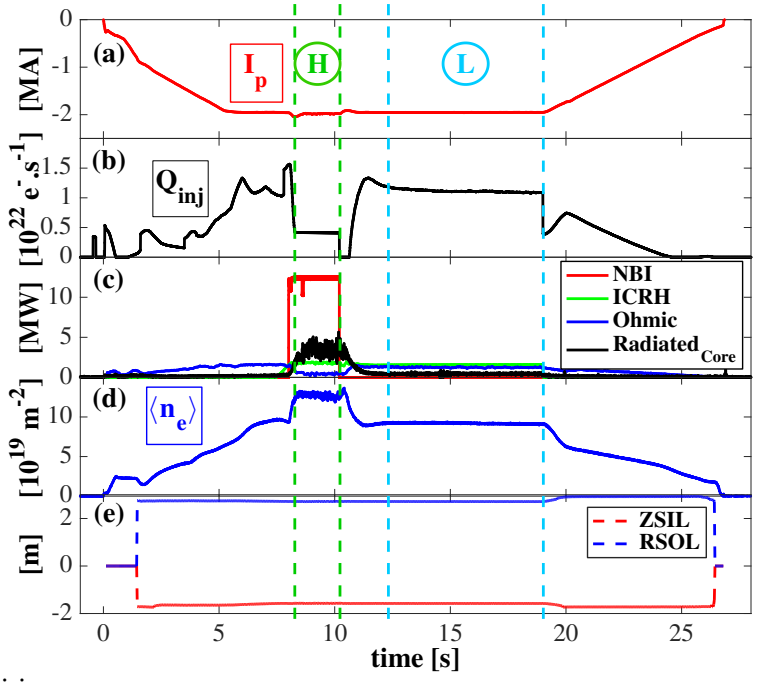

Figure 1: Time evolution of pulse parameters for #JPN89044: (a) plasma current I_p, (b) gas puff injection rate Q_{inj}, (c) input and radiated powers, (d) line-integrated electron density $\langle n_e \rangle$, (e) inner strike point vertical position $ZSIL$ and outer strike point horizontal position $RSOL$ (cf. figure 2 for the JET coordinates). Two steady-state phases, labelled H (for H-mode) and L (for L-mode), are identified. They are characterised by constant pulse parameters.

From figure 1, the two steady-state plasma phases are clearly identified. They are defined by constant magnetic equilibrium (X-point configuration and strike-points location), particle injection rate, heating

power and plasma density:
(1) H-mode phase: from 8.3 s to 10.3 s. 15 MW of total heating power is injected in the plasma. The Neutral Beam Injection (NBI) contribution, P_{NBI}, is 12.5 MW, the Ion Cyclotron Resonance Heating (ICRH) contribution, P_{ICRH}, is 2 MW and the Ohmic contribution, P_{Ohm} is 0.5 MW. The plasma is fuelled from the bottom of the inner divertor with a puff injection rate, Q_{inj}, of 4.1×10^{21} D.s^{-1}. The NBI also fuels the plasma from the core with an injection rate, Q_{NBI}, of 1.5×10^{21} D.s^{-1} (not shown in figure 1, constant injection during this phase). The upstream line-integrated electron density $\langle n_{\mathrm{e}} \rangle$ is 1.2×10^{20} m^{-2}. In the following, only the inter-ELM plasma conditions will be considered.
(2) L-mode phase: from 12 s to 19 s. 2.9 MW of total heating power ($P_{\mathrm{ICRH}} = 1.6$ MW and $P_{\mathrm{Ohm}} =$ 1.3 MW). Deuterium is injected from the tokamak outer midplane with an injection rate of 4.1×10^{21} D.s^{-1} and from the top of the machine with an injection rate of 6.9×10^{21} D.s^{-1} (both with density feedback). The upstream line-integrated electron density $\langle n_{\mathrm{e}} \rangle$ is 9.2×10^{19} m^{-2}.

Due to the impossibility to simulate the plasma ramp-up and ramp-down phases with SolEdge-EIRENE, only the H-mode and L-mode phases will be assumed to be relevant in estimating the overall plasma-wall interaction of this discharge. Please notice that this assumption is strong and probably wrong. Indeed, both of them only represent 35 % of the pulse duration (65 % of the duration of the plasma current flat-top phase). However, almost 60 % of the total integrated ion fluence on the divertor measured by Langmuir probes is deposited during this two phases [13]. This percentage increases to 72 % if only the flat-top phase is considered. This indicates that most of the integrated fluence of the discharge is deposited during the H-mode and L-mode phases. Thus, the considered assumption seems reasonable.

3 Backgrounds for the two plasma phases and evolution of the implantation conditions.

The SolEdge-EIRENE edge-plasma transport code has the capability to calculate the plasma conditions at the wall in complex geometry. It can provide, among others, the local implantation quantities all along the wall of fusion devices, i.e. the flux density of implanted HI Γ_{imp} [m^{-2}.s^{-1}], their mean impact energy E_{imp} [eV], their mean angle of incidence w.r.t. the surface α_{imp} [°] and the net heat flux density Φ_{net} [W.m^{-2}]. Such quantities are provided as a function of the curvilinear coordinate s defined in figure 2 in the case of the JET device.
In the following, the two H-mode and L-mode phases are simulated with SolEdge-EIRENE. The settings for both simulations are detailed in Appendix A. For the H-mode, only the inter-ELM plasma is simulated since the modelling of the ELM transients is not conceivable due to its computational cost. These simulations converged to a stationary state, providing the plasma profiles at the wall required by DWE. The profiles of the implanted particle flux density Γ_{imp}, the impact energy E_{imp} and the net heat flux density Φ_{net} are plotted in figure 3 for the H-mode and L-mode phases along the wall of the JET tokamak versus the s curvilinear coordinate. As the angle of incidence does not clearly change between the two phases (it remains around 70° and 45° for the ions and atoms), no clear impact of α_{imp} is expected on the wall dynamics and it is not displayed in the following. The main results are:

- *Implanted particle flux density* Γ_{imp}: interestingly, it displays no significant difference in the first-wall between the H-mode and L-mode phases, and Γ_{imp} is of the same order of magnitude for both ions and atoms. In the divertor, Γ_{imp} is one to two orders of magnitude higher than on the first-wall; the ionic contribution is higher than the atomic contribution during the H-mode phase, while the reverse situation occurs during the L-mode phase. A sharp increase of the atom flux density is noted everywhere in the divertor during the L-mode phase as the divertor is in detached regime. For both phases, Γ_{imp} varies along the curvilinear coordinate s, notably at the strike points where two peaks are observed for ions during the H-mode and for atoms during the L-mode. These variations are analysed later on in this section.

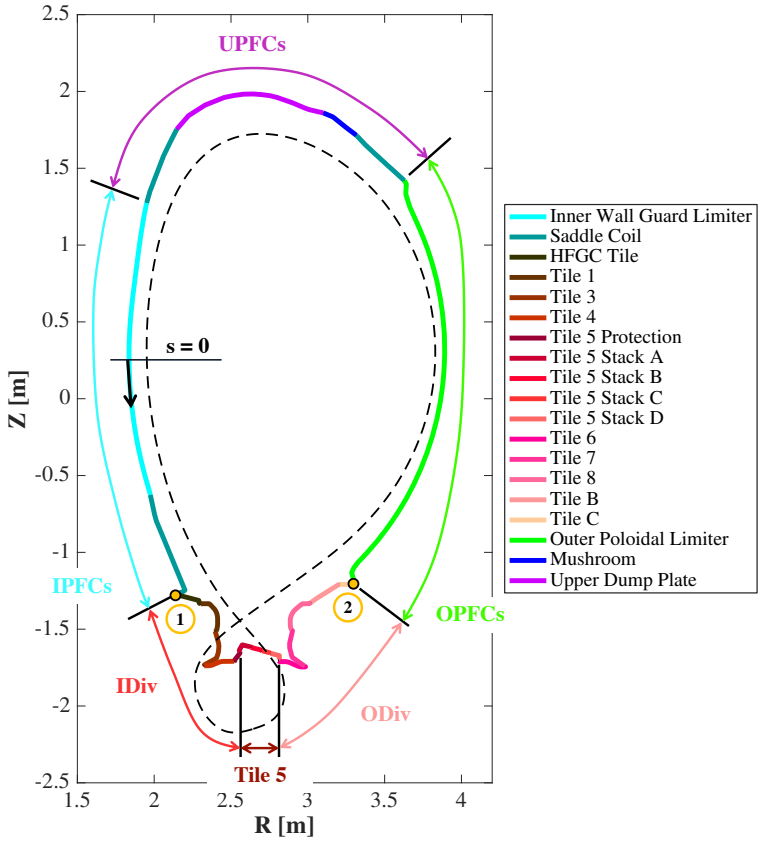

Figure 2: Poloidal cross-section of the JET tokamak with the different PFCs considered in the simulation presented in this article. Points 1 and 2 indicate the boundary between the two regions of the vacuum vessel: from 1 $\rightarrow$ 2 clockwise the first-wall, from 2 $\rightarrow$ 1 the divertor. The curvilinear coordinate along the wall, s, is introduced. Six zones in the wall are also defined: the Inner Divertor zone (IDiv), the Tile 5 zone, the Outer Divertor zone (ODiv), the Outer PFCs (OPFCs), the Upper PFCs (UPFCs) and the Inner PFCs (IPFCs). In the following, these zones will be used to display integrated or mean simulation results. Three zones are made with Saddle Coil PFCs. They will be referred to as *Inner Lower Protection*, *Outer Upper Protection* and *Inner Upper Protection*.

- *Impact energy* E_{imp}: the impact energy of D atoms and ions is notably lower in the L-mode. This is a consequence of the decrease in injected power with respect to the H-mode. This difference is stark at the divertor where E_{imp} is one to two order of magnitude higher in the H-mode than in the L-mode as the divertor regime goes from attached to detached. This difference is even more pronounced at the strike points for the D^+ ions which impact energy can reach up to $\sim$ 600 eV during the H-mode as the result of the high plasma temperature there. Again, the spatial variations of E_{imp} are analysed below.

- *Net heat flux density* Φ_{net}: during the H-mode, one can note excursions of Φ_{net} up to 4.2 MW.m^{-2} and 5.9 MW.m^{-2} at the inner and outer strike-points, respectively. As a consequence, strong heating of the surface material is expected there. Otherwise, the heat flux density remains below 0.1 MW.m^{-2} on all the first-wall, the outer vertical target and the private flux region, with moderate excursions up to $\sim$ 0.3 MW.m^{-2} in the inner far Scrape-Off Layer. Similarly in the L-mode, Φ_{net} remains below 0.1 MW.m^{-2} except at the strike-points where nevertheless it does not exceed 0.2 MW.m^{-2}. It follows that no heating of the PFCs materials is expected in these

conditions.

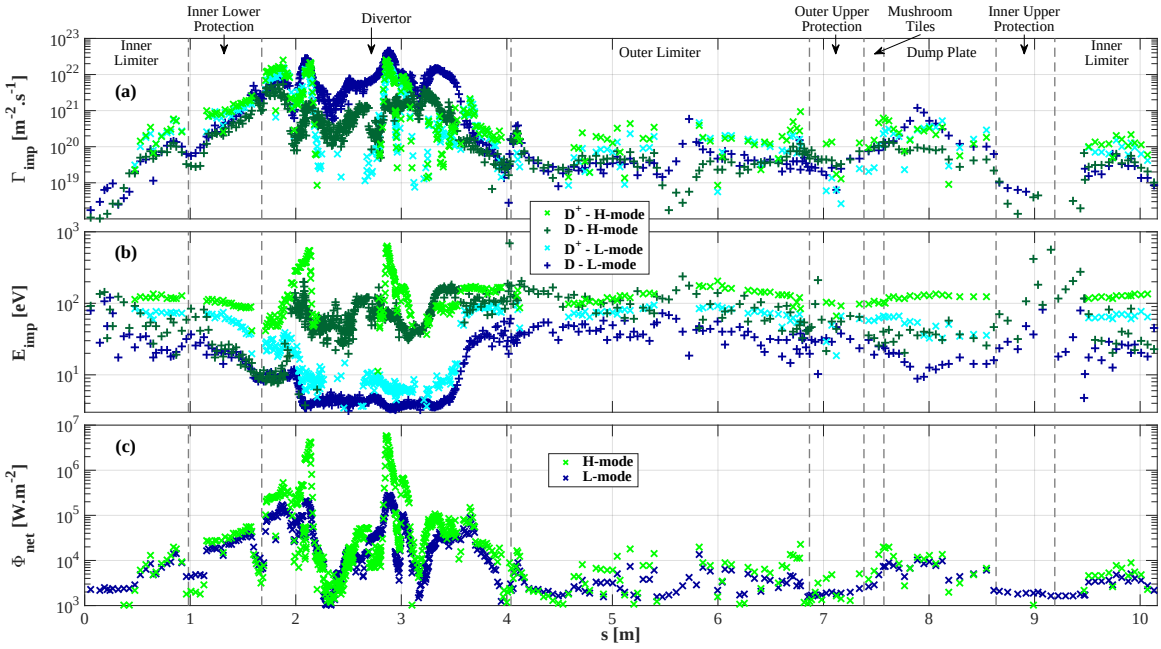

Figure 3: SolEdge-EIRENE simulation results for both H-mode phase and L-mode phase: distribution along the wall of (a) the implanted particle flux density Γ_{imp}, of (b) the impact energy E_{imp} and of (c) the net heat flux density Φ_{net}. These quantities are required as inputs for the DWE module. The first two quantities are plotted for both deuterium ions and atoms. The definition of the s curvilinear coordinate can be found in figure 2.

To verify the consistency of the plasma conditions at both divertor targets, these simulations have been confronted to the experimental measurements available (cf. reference [13]). The simulated saturation current density J_{sat} profiles at the divertor are consistent with the experimental ones measured by Langmuir probes, except for the H-mode phase where the inner experimental profile is higher. The simulations provide a good estimate of the incident ion flux at the divertor during the plasma current flat-top phase of #JPN89044. However, no conclusion can be drawn on the resulting implantation quantities (flux density and impact energy) in the experiment due to the lack of estimation of the electron temperature from Langmuir probes data. Moreover, no measurements were performed in the first-wall during this campaign.

As it was observed in figure 3, the H-mode and the L-mode phases induce strongly different plasma-wall interactions. Moreover, these interactions exhibit strong variations along the s coordinate on the tokamak wall. This implies different wall dynamics depending on the location at the wall and on the plasma phase. In order to help in the analysis of these dynamics, the JET wall is arbitrarily divided in six different zones below (cf. figure 2) (three zones for the divertor, three for the first-wall). For each zone, the mean values of the ion and atom contributions to Γ_{imp} and E_{imp} are given in table 1, 2, 3, 4 and commented below:

- *Implanted particle flux density* $\Gamma_{\mathrm{imp}}^{\mathrm{mean}}$: the ion flux density $\Gamma_{\mathrm{imp}}^{\mathrm{i+,mean}}$ is of the same order of magnitude between the H-mode and the L-mode in all the zones of the tokamak. Overall, it is lower in the L-mode phase with ratios $\Gamma_{\mathrm{imp,L}}^{\mathrm{i+,mean}}/\Gamma_{\mathrm{imp,H}}^{\mathrm{i+,mean}}$ ranging from 0.49 to 0.67 at the divertor (table 1), and from 0.63 to 0.81 at the first-wall (table 2). The atom flux density $\Gamma_{\mathrm{imp}}^{\mathrm{at,mean}}$ is higher

in the L-mode with $\Gamma^{\mathrm{at,mean}}_{\mathrm{imp,L}}/\Gamma^{\mathrm{at,mean}}_{\mathrm{imp,H}}$ ratios ranging from 2.8 up to 19 at the divertor (table 1) and from 1.5 to 3.0 at the first-wall (table 2). Overall, once both ionic and atomic contributions to $\Gamma^{\mathrm{mean}}_{\mathrm{imp}}$ are considered, the global particle ratio $\Gamma^{\mathrm{mean}}_{\mathrm{imp,L}}/\Gamma^{\mathrm{mean}}_{\mathrm{imp,H}}$ remains close to unity.

- *Impact energy* $E^{\mathrm{mean}}_{\mathrm{imp}}$: $E^{\mathrm{mean}}_{\mathrm{imp}}$ displays the same trend for its ionic and atomic contributions in all six zone of the tokamak. The ratio $E^{\mathrm{mean}}_{\mathrm{imp,L}}/E^{\mathrm{mean}}_{\mathrm{imp,H}}$ below one is also very similar for each zone between both ionic and atomic contribution. Overall, it can be concluded to a significant drop of $E^{\mathrm{mean}}_{\mathrm{imp}}$ from the H-mode to the L-mode everywhere on the tokamak wall.

		Inner Divertor			Tile 5			Outer Divertor		
		Total	Ions	Atoms	**Total**	Ions	Atoms	**Total**	Ions	Atoms
$\Gamma^{\mathrm{mean}}_{\mathrm{imp}}$ [10^{20} D.m^2.s^{-1}]	H-mode	98.9	85.9	13.0	92.9	84.0	8.88	17.5	11.0	6.49
	L-mode	118	55.7	62.8	211	41.3	170	49.3	7.34	42.0
$\frac{\Gamma^{\mathrm{mean}}_{\mathrm{imp,L}}}{\Gamma^{\mathrm{mean}}_{\mathrm{imp,H}}}$		**1.2**	0.65	4.8	**2.3**	0.49	19	**2.8**	0.67	6.5

Table 1: Mean implantation flux density ($\Gamma^{\mathrm{mean}}_{\mathrm{imp}}$) in the three different zones of the divertor (defined in figure 2) during both H-mode and L-mode phases. The ions and atoms contribution to the total implantation flux density is reported. The ratio between the L-mode and the H-mode flux densities, $\Gamma^{\mathrm{mean}}_{\mathrm{imp,L}}/\Gamma^{\mathrm{mean}}_{\mathrm{imp,H}}$, is also indicated.

		Outer PFCs			Upper PFCs			Inner PFCs		
		Total	Ions	Atoms	**Total**	Ions	Atoms	**Total**	Ions	Atoms
$\Gamma^{\mathrm{mean}}_{\mathrm{imp}}$ [10^{20} D.m^2.s^{-1}]	H-mode	1.92	1.52	0.408	2.52	1.97	0.548	6.70	5.11	1.59
	L-mode	1.56	0.959	0.605	3.26	1.62	1.64	6.85	4.04	2.81
$\frac{\Gamma^{\mathrm{mean}}_{\mathrm{imp,L}}}{\Gamma^{\mathrm{mean}}_{\mathrm{imp,H}}}$		**0.81**	0.63	1.5	**1.3**	0.82	3.0	**1.0**	0.79	1.8

Table 2: Mean implantation flux density ($\Gamma^{\mathrm{mean}}_{\mathrm{imp}}$) in the three different zones of the first-wall (defined in figure 2) during both H-mode and L-mode phases. The ions and atoms contribution to the total implantation flux density is reported. The ratio between the L-mode and the H-mode flux densities, $\Gamma^{\mathrm{mean}}_{\mathrm{imp,L}}/\Gamma^{\mathrm{mean}}_{\mathrm{imp,H}}$, is also indicated.

		Inner Divertor		Tile 5		Outer Divertor	
		Ions	Atoms	Ions	Atoms	Ions	Atoms
$E^{\mathrm{mean}}_{\mathrm{imp}}$ [eV]	H-mode	164	52.6	247	77.4	136	114
	L-mode	18.6	6.46	7.55	4.04	50.3	19.5
$\frac{E^{\mathrm{mean}}_{\mathrm{imp,L}}}{E^{\mathrm{mean}}_{\mathrm{imp,H}}}$		0.11	0.12	0.031	0.052	0.37	0.17

Table 3: Mean impact energy ($E^{\mathrm{mean}}_{\mathrm{imp}}$) in the three different zones of the divertor (defined in figure 2) during both H-mode and L-mode phases. The ratio between the L-mode and the H-mode energies, $E^{\mathrm{mean}}_{\mathrm{imp,L}}/E^{\mathrm{mean}}_{\mathrm{imp,H}}$, is also indicated.

As a summary of this section, the transition from the H-mode phase to the L-mode phase induces almost no changes in the overall particle flux densities while it is accompanied by a significant drop in the impact energy. In the following sections, the impact of such variation on the wall dynamics will be analysed through modelling via the DWE code.

		Outer PFCs		Upper PFCs		Inner PFCs	
		Ions	Atoms	Ions	Atoms	Ions	Atoms
$E_{\mathrm{imp}}^{\mathrm{mean}}$ [eV]	H-mode	133	107	115	68.4	115	62.6
	L-mode	76.2	41.1	50.5	24.6	65.8	28.5
$\frac{E_{\mathrm{imp,L}}^{\mathrm{mean}}}{E_{\mathrm{imp,H}}^{\mathrm{mean}}}$		0.57	0.38	0.44	0.36	0.57	0.46

Table 4: Mean impact energy ($E_{\mathrm{imp}}^{\mathrm{mean}}$) in the different zones of the first-wall (defined in figure 2) during both H-mode and L-mode phases. The ratio between the L-mode and the H-mode energies, $E_{\mathrm{imp,L}}^{\mathrm{mean}}/E_{\mathrm{imp,H}}^{\mathrm{mean}}$, is also indicated.

4 The Dynamics of Wall Elements module.

The DWE wall module is developed to communicate with SolEdge-EIRENE. DWE is based on two internal codes, WE-temp and MHIMS [13]. WE-temp determines the wall temperature based on the heat flux density Φ_{net} on the wall surface, while MHIMS models the implantation, transport, trapping of hydrogen isotopes in the materials and their desorption based on $\Gamma_{\mathrm{imp}}^{j}$, E_{imp}^{j}, $\alpha_{\mathrm{imp}}^{j}$ and the temperature of the wall element. Here the superscript j denotes the nature of the interacting particle (ion or atom).
How DWE operates is briefly sketched in figure 4: EIRENE provides Φ_{net}, $\Gamma_{\mathrm{imp}}^{j}$, E_{imp}^{j}, and $\alpha_{\mathrm{imp}}^{j}$ as input data to DWE. These input data are provided depending on the time t and location s at the wall surface of the tokamak. At every time step, WE-temp and MHIMS are run on each wall element/cell. DWE's outputs are the wall temperature (also used as input by MHIMS), the density of mobile particles n_{m}, the density of trapped hydrogen isotopes $n_{\mathrm{t},i}$ (where the lower-script i denotes the type of trap), and the outgassing flux density Γ_{out}.
In addition to the communication between the different codes, DWE also manages their parallelisation through OpenMP. As WE-temp and MHIMS consider only one dimension perpendicular to the s coordinate, two neighbouring elements on the wall are independent. This enables both codes to be numerically parallelised in the $\vec{s}$ direction and to run DWE on several CPUs. As an example, for the case presented in this article, the wall is made of 691 elements.
In the following, the WE-temp and MHIMS internal codes are briefly described.

4.1 Thermal model: WE-temp

The WE-temp thermal model is based on the following assumptions:
(1) The complex geometry and the design of the PFC are approximated by a multi-layer slab geometry.
(2) The material thermal properties are assumed to be constant with the temperature and to be isotropic.
(3) Thermal radiation from the PFC surfaces is neglected and the lateral surfaces are considered insulating.
(4) The net heat flux density Φ_{net} is considered uniform.

A sketch of the considered slab geometry is shown in figure 5. The slab is defined by the L_x, L_y and L_z lengths. Due to the moderate L_y length, the PFC $\vec{y}$ direction is aligned with the local SolEdge-EIRENE wall curvilinear $\vec{s}$ direction. As the heat flux density is considered uniform over the PFC, a calculation of the mean temperature in both $\vec{y}$ and $\vec{z}$ directions is performed. Actively-cooled PFCs are modeled by considering a convective boundary condition with a coolant at a temperature T_{cool} at the rear surface (at $x = L_x$). For inertially-cooled PFCs, a similar boundary condition is imposed with a very low heat convection coefficient to mimic the PFC cooling due to heat diffusion into the tokamak structure. In that case, the initial uniform PFC temperature at the beginning of a day of operation, T_0, is considered for the boundary condition.

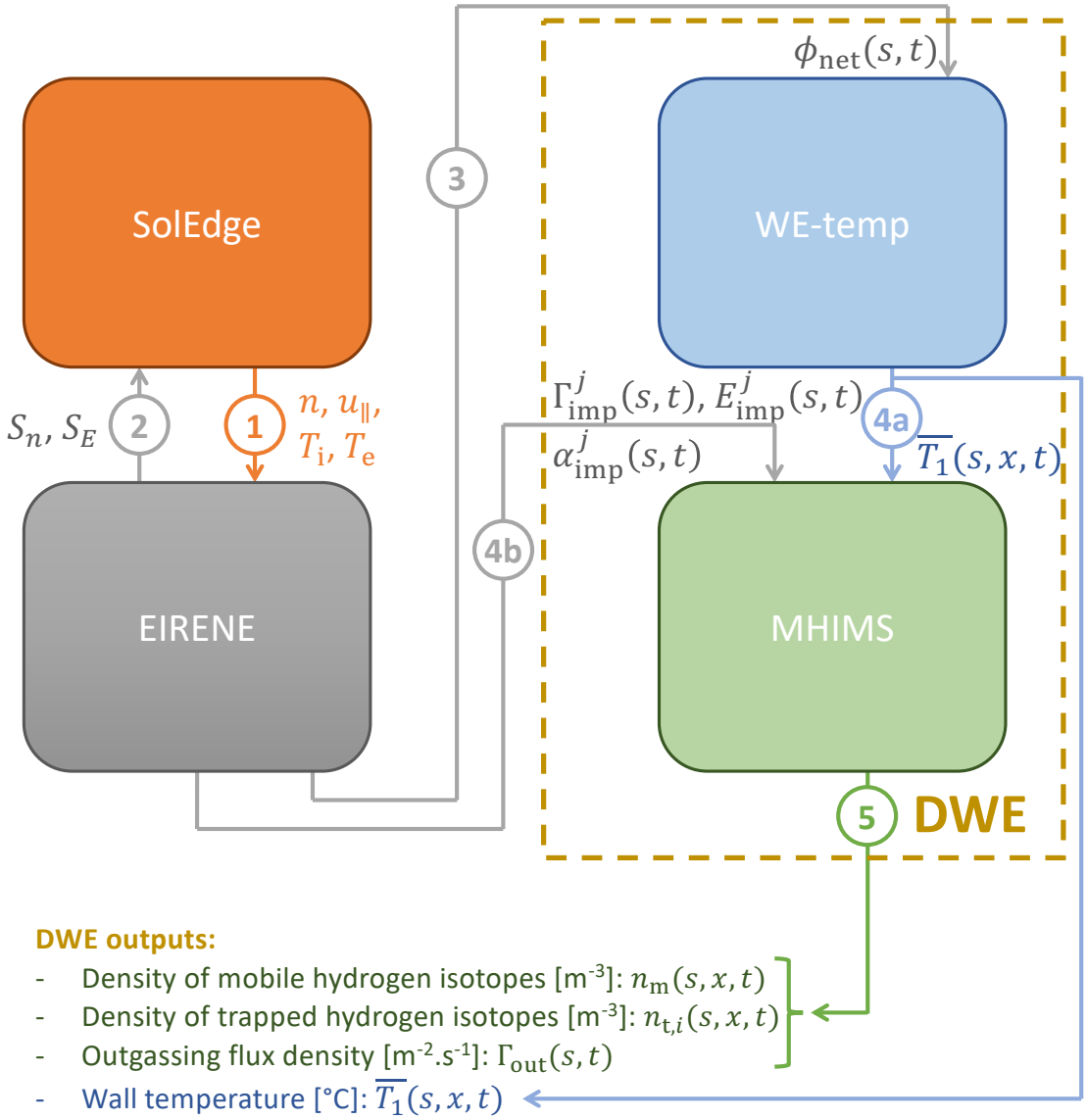

Figure 4: Architecture of the interaction between DWE and SolEdge-EIRENE.

The temperature profile in the PFCs is computed by solving the 1D heat equation in the depth material through the so-called Duhamel integral of superposition [14]:

$$\overline{T_i}(s,x,t) = T_i(s,x,0) + \int_0^t \Phi_{\text{net}}(s,\tau)\frac{\partial T_i^{\text{step}}(s,x,t-\tau)}{\partial t}\,d\tau \tag{1}$$

where $\overline{T_i}(s,x,t)$ is the temperature in the material layer number i averaged in the toroidal direction [°C] and $T_i(s,x,0)$ is the initial layer temperature [°C]. T_i^{step} is the PFC temperature response to a

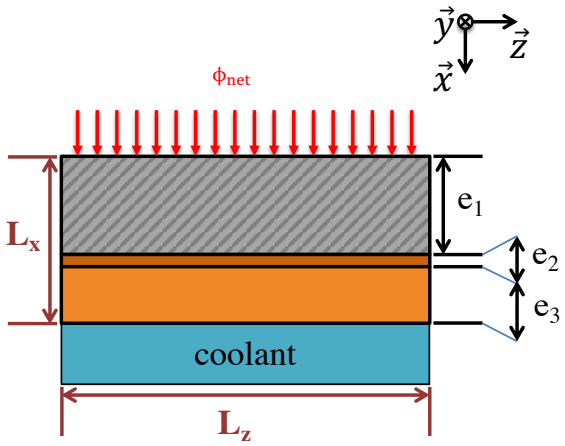

Figure 5: Schematics of the PFC simplified slab geometry considered in WE-temp. The PFC is made of a superposition of material layers (three different layers in this example). Actively-cooled PFCs are modeled by considering a convective boundary condition with a coolant at a temperature T_{cool} at the rear surface (at $x = L_x$). For inertially-cooled PFCs, a similar boundary condition is imposed with a very low heat convection coefficient to mimic the PFC cooling due to heat diffusion into the tokamak structure. In that case, the initial uniform PFC temperature at the beginning of a day of operation, T_0, is considered for the boundary condition.

unit heat flux density step [°C.(W.m^{-2})$^{-1}$], solution of the following auxiliary problem:

$$\begin{cases} \rho_i c_{p_i} \dfrac{\partial T_i^{\text{step}}(s,x,t)}{\partial t} = \lambda_i \dfrac{\partial^2 T_i^{\text{step}}}{\partial x^2} & \text{(2a)} \\ \text{B.C. at } x = x_0 = 0\text{: } -\lambda_1 \dfrac{\partial T_1^{\text{step}}}{\partial x}(s,0,t) = 1 & \text{(2b)} \\ \text{B.C. at } x = x_i = \displaystyle\sum_{j=1}^{i<N} e_j\text{: } \begin{aligned} -\lambda_i \frac{\partial T_i^{\text{step}}}{\partial x}(s,x_i,t) &= \frac{1}{R_{c_i}} \times \left[T_i^{\text{step}}(s,x_i,t) - T_{i+1}^{\text{step}}(s,x_i,t)\right] \\ &= -\lambda_{i+1} \frac{\partial T_{i+1}^{\text{step}}}{\partial x}(s,x_i,t) \end{aligned} & \text{(2c)} \\ \text{B.C. at } x = x_N\text{: } -\lambda_N \dfrac{\partial T_N^{\text{step}}}{\partial x}(s,L_x,t) = h T_N^{\text{step}}(s,L_x,t) & \text{(2d)} \\ \qquad\qquad = L_x & \\ \text{I.C.: } T_i^{\text{step}}(s,x,0) = 0 & \text{(2e)} \end{cases}$$

where B.C. are the boundary conditions and I.C. is the initial condition. All the parameters and variables of the system 2 are given in table 5.
Now the net heat flux density Φ_{net}, provided by SolEdge-EIRENE, is decomposed in a series of $N_\phi(s,t)$ step changes $\Delta\phi_k$ [W.m^{-2}] at time t_k:

$$\Phi_{\text{net}}(s,t) = \sum_{k=1}^{N_\phi(s,t)} \Delta\phi_k(s)\mathcal{H}(t - t_k(s)) \tag{3}$$

where $\mathcal{H}$ is the Heaviside step function. After some algebra, detailed in Appendix B, the general

Variable or parameter	Definition	Units
s	Wall coordinate	m
x	Material depth	m
t	Time	s
$\overline{T_i}(s,x,t)$	Temperature in the material i averaged in the toroidal direction	°C
$T_i(s,x,0)$	Initial PFC temperature	°C
$\Phi_{\text{net}}(s,t)$	Net heat flux density	W.m^{-2}
$T_i^{\text{step}}(s,x,t)$	PFC temperature response to a unit heat flux density step	$\text{°C.(W.m}^{-2})^{-1}$
λ_i	Thermal conductivity of material i	$\text{W.m}^{-1}\text{.°C}^{-1}$
c_{p_i}	Specific heat of material i	$\text{J.kg}^{-1}\text{.°C}^{-1}$
ρ_i	Mass density of material i	kg.m^{-3}
R_{c_i}	Contact resistance of the interface between material i and material $i+1$	$\text{°C.(W.m}^{-2})^{-1}$
e_i	Thickness of material layer i	m

Table 5: Variables and parameters of the heat equation 1 and its auxiliary problem equation 2.

equation of WE-temp is obtained:

$$\begin{cases} \overline{T_i}(s,x,t) = T_i(s,x,0) + \sum_{k=1}^{N_\phi(s,t)} \Delta\phi_k(s) T_i^{\text{step}}(s,x,t-t_k(s)) & \text{(4a)} \\ T_i(s,x,0) = T_{\text{cool}}(s) \text{ for actively-cooled PFCs} & \text{(4b)} \\ T_i(s,x,0) = T_0(s) \text{ for inertial PFCs} & \text{(4c)} \end{cases}$$

In equation 4a, the initial temperature $T_i(s,x,0)$ is equal to the cooling temperature T_{cool} for actively-cooled PFCs. For inertial PFCs, $T_i(s,x,0)$ is equal to the PFC temperature at the beginning of a day of operation, T_0. Please note that in equation 4, T_{cool}, T_0 and T_i^{step} are function of the variable s as they depend on the PFC which is in the position s on the wall. In the end, provided that an analytical or semi-analytical calculation of the PFC step response is possible, equation 4 gives the temperature profile in the zone simulated in MHIMS (limited to the material layer at the surface) without calculating the temperature profile in the whole PFC. Indeed, this profile, as well as the PFC design (material layers and cooling technique), are accounted in the calculation of the step response. This calculation is made using the so-called quadrupole method [15, 16] and is detailed in appendix C. This method gives the temperature in the Laplace space, equation 41, which is then inverted using the inversion formula 10 to go back to the time space. This integral cannot be calculated analytically but can be estimated numerically using an appropriate algorithm. In WE-temp, such inversion is done using the De Hoog's algorithm [17].

4.2 Hydrogen isotopes – Material interaction model: MHIMS.

In DWE, the model of HI–Material interaction is based on the code MHIMS (Migration of Hydrogen Isotopes in MaterialS) [18]. This code relies on the so-called Reaction-Diffusion system of equations to describe the transport and trapping of HI in the bulk of materials originally introduced by McNabb and Foster in 1963 [19]. Since then, it has been widely used and the MHIMS code has also been largely described in previous publications [18, 20]. In brief, two HI populations are considered: the mobile HI, which can diffuse in the material through interstitial sites, and the HI which are trapped in the lattice defects. These defects, also called traps, are considered as saturable and can only accommodate a single HI. They can be intrinsic (i.e. due to the manufacturing process) like grain boundaries and impurities, or extrinsic, i.e. due to the plasma or neutron irradiation, like vacancies or bubbles. The Reaction-Diffusion model expresses the time evolution of the density of mobile HI, n_{m} [m^{-3}], and of the density of trapped HI at the trap of kind i, $n_{\text{t},i}$ [m^{-3}]. It couples a diffusion equation for the mobile particles, equation 5a, to trapping-detrapping equations in various traps of kind i according to

the reaction $\mathrm{HI_m} + \mathrm{Trap}_i \leftrightarrows \mathrm{HI}_{\mathrm{t},i}$, equation 5b:

$$\begin{cases} \dfrac{\partial n_{\mathrm{m}}(s,x,t)}{\partial t} = \dfrac{\partial}{\partial x}\left(D\big(s,\overline{T_1}\big)\,\dfrac{\partial n_{\mathrm{m}}}{\partial x}\right) - \displaystyle\sum_{i=1}^{N_{\mathrm{trap}}(s)} \dfrac{\partial n_{\mathrm{t},i}}{\partial t} & \text{(5a)} \\ \qquad\qquad + S^{\mathrm{i+}}_{\mathrm{ext}}(s,x,t) + S^{\mathrm{at}}_{\mathrm{ext}}(s,x,t) \\ \dfrac{\partial n_{\mathrm{t},i}(s,x,t)}{\partial t} = \nu^{*}_{\mathrm{t},i}(s,\overline{T_1})\dfrac{n_i(s,x)-n_{\mathrm{t},i}}{n_{\mathrm{IS}}(s)} n_{\mathrm{m}} - \nu_{\mathrm{dt},i}(s,\overline{T_1}) n_{\mathrm{t},i} & \text{(5b)} \\ \text{B.C. at } x=0\text{: } n_{\mathrm{m}}(s,0,t) = 0 & \text{(5c)} \\ \text{B.C. at } x=L\text{: } \begin{vmatrix} n_{\mathrm{m}}(s,L,t) = 0 \\ \text{or} \\ D(s,T)\dfrac{\partial n_{\mathrm{m}}}{\partial x}(s,L,t) = 0 \end{vmatrix} & \text{(5d)} \end{cases}$$

All the parameters and variables of this system of equations are given in table 6. In DWE, it is solved in the surface materials.

Variable or parameter	Definition	Units
s	Wall coordinate	m
x	Material depth	m
t	Time	s
$\overline{T_1}(s,x,t)$	Mean temperature in the surface material	°C
$n_{\mathrm{m}}(s,x,t)$	Density of mobile HI	m^{-3}
$D\big(s,\overline{T_1}\big) = D_0(s)\exp\big(-E_{\mathrm{diff}}(s)/\big(k_{\mathrm{B}}\overline{T_1}\big)\big)$	Diffusion coefficient of HI in the material	$\mathrm{m}^2.\mathrm{s}^{-1}$
$E_{\mathrm{diff}}(s)$	Activation energy of diffusion	eV
k_{B}	Boltzmann constant	$\mathrm{eV}.°\mathrm{C}^{-1}$
$N_{\mathrm{trap}}(s)$	Number of traps in the material	
$n_{\mathrm{t},i}(s,x,t)$	Density of trapped HI at the trap of kind i	m^{-3}
$\nu^{*}_{\mathrm{t},i}\big(s,\overline{T_1}\big) = \nu^{0}_{\mathrm{t},i}(s)\exp\big(-E_{\mathrm{t},i}(s)/\big(k_{\mathrm{B}}\overline{T_1}\big)\big)$	Trapping attempt frequency in the trap of kind i	s^{-1}
$E_{\mathrm{t},i}(s)$	Activation energy of trapping	eV
$n_i(s,x)$	Density of trap of kind i	m^{-3}
$n_{\mathrm{IS}}(s)$	Density of interstitial sites for HI	m^{-3}
$\nu_{\mathrm{dt},i}\big(s,\overline{T_1}\big) = \nu^{0}_{\mathrm{dt},i}(s)\exp\big(-E_{\mathrm{dt},i}(s)/\big(k_{\mathrm{B}}\overline{T_1}\big)\big)$	Detrapping frequency	s^{-1}
$E_{\mathrm{dt},i}(s)$	Activation energy of detrapping	eV
$S^{\mathrm{i+}}_{\mathrm{ext}}(s,x,t)$	Implantation source of HI ions	$\mathrm{m}^{-3}.\mathrm{s}^{-1}$
$S^{\mathrm{at}}_{\mathrm{ext}}(s,x,t)$	Implantation source of HI atoms	$\mathrm{m}^{-3}.\mathrm{s}^{-1}$

Table 6: Variables and parameters of the MHIMS equations.

One can note that the following parameters are function of s: D, N_{trap}, $\nu^{*}_{\mathrm{t},i}$, $\nu_{\mathrm{dt},i}$, n_i, and n_{IS}. Indeed, these quantities are all material dependent and the s dependence of these quantities is here to indicate the different materials considered along the wall.
In equation 5a, implantation of ions and atoms from the plasma are given by two volume source, $S^{\mathrm{i+}}_{\mathrm{ext}}$ and $S^{\mathrm{at}}_{\mathrm{ext}}$ respectively:

$$S^{j}_{\mathrm{ext}}(s,x,t) = \Gamma^{j}_{\mathrm{imp}}(s,t) f^{j}_{\mathrm{imp}}(E^{j}_{\mathrm{imp}}(s,t), \alpha^{j}_{\mathrm{imp}}(s,t)) \tag{6}$$

where $\Gamma^{j}_{\mathrm{imp}}$ is the particle implantation flux density provided by SolEdge-EIRENE and f^{j}_{imp} is the implantation profile. It is considered as a gaussian defined by a mean implantation range of particles and a standard deviation. Both parameters depend on the impact energy E^{j}_{imp} and on the angle of incidence $\alpha^{j}_{\mathrm{imp}}$. In MHIMS, these gaussian parameters are given by tables calculated with the Binary Collision Approximation code SRIM [21].

The system of equations 5 is solved considering Boundary Conditions (B.C.) at both front ($x = 0$) and rear ($x = L$) surfaces. We here consider that HI recombination and desorption are instantaneous at $x = 0$, yielding to the Dirichlet B.C equation 5c. On the rear side, either Dirichlet or Neumann B.C., equations 5d, is assumed depending on the material.
The MHIMS equations considered in DWE are based on several approximations. First, the diffusion of HI is one-dimensional in equation 5a. This approximation is appropriate since, in fusion devices, the gradient length of the plasma flux density at the surface of materials (of the order of millimeters to centimeters) is larger than the characteristic depth of diffusion of HI in the depth of the materials on the time scales of usual plasma discharges in present machines (typically of order of micrometers to millimeters). Therefore, the transport of HI in materials remains one-dimensional, in the direction of the depth of the materials $\vec{x}$. One can also note that the traps density n_i is not function of time. n_i can evolve with time due to the creation of traps, their diffusion and their annihilation. The modelling of all these processes would require solving other partial differential equations with new free parameters (diffusion coefficients, reaction rates, etc.) that would add complexity to the model. Therefore one assumes that the traps creation has saturated, or that the characteristic time of the creation is high w.r.t. the time of simulation. One also assumes that traps are immobile and cannot annihilate.
According to the DWE coupling architecture, figure 4, $\Gamma^j_{\text{imp}}(s,t)$, $E^j_{\text{imp}}(s,t)$ and $\alpha^j_{\text{imp}}(s,t)$ are provided to MHIMS by SolEdge-EIRENE (cf. figure 4). Moreover, diffusion, trapping and detrapping are thermally-activated processes. To calculate the diffusion coefficient, the trapping frequency and detrapping frequency, the temperature profile in the surface materials calculated by WE-temp is considered in MHIMS (cf. section 4.1).

5 Simulation of retention dynamics during four consecutive similar discharges with H-mode to L-mode transition with the DWE code.

SolEdge-EIRENE simulations allow to determine the two sets of input parameters (Γ_{imp}, E_{imp}, α_{imp}, and Φ_{net}) to DWE for each of the H-mode and L-mode phases. The duration of each phase is 2 s for the H-mode and 7 s for the L-mode, as in the experimental discharge #JPN89044 presented in section 2. The initial D density in the wall is set to zero. Four successive pulses followed by 30 min resting time are simulated. Figure 6 exhibits the time evolution of the total implantation flux on the JET wall, $Q_{\text{imp,tot}}$ [at.s^{-1}], during this simulation. The four peaks indicate the plasma discharges. A zoom on the first discharge is also shown in inlet to focus on the $Q_{\text{imp,tot}}$ behaviour during the H-mode phase and the L-mode phases.
Only four discharges are simulated as it was shown that the retention dynamics was similar from the third discharge (cf. reference [7]). Such a behaviour is consistent with experimental observations in metallic tokamaks like JET-ILW [1, 2]. It indicates that the wall is initialised in terms of dynamic retention: the traps responsible for long-term retention, initially empty, are being saturated up to a sufficient depth so that their impact on the retention during discharge is negligible.

5.1 Plasma facing components and materials considered in DWE.

The parameters used in the DWE simulation are defined in the following.

Parameters for WE-temp:
JET-ILW tokamak is composed of inertially-cooled PFCs. In WE-temp, such PFCs are simulated like actively-cooled PFCs with a very low heat convection coefficient (100 W.m^{-2}.°C^{-1}). This enables the model to mimic the cooling of the PFCs by radiation and by heat conduction into the tokamak structure between the discharges, while keeping their inertial behaviour during plasma exposure. JET-ILW has 19 different PFCs which are distributed in 22 different zones in the vacuum vessel (cf. figure

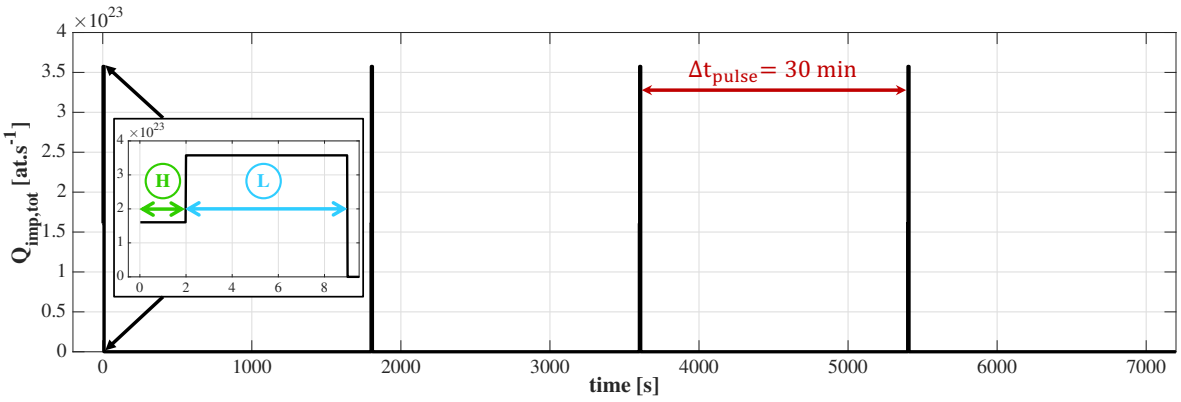

Figure 6: Time evolution of the total implantation flux $Q_{\mathrm{imp,tot}}$ considered in the following simulation. The four consecutive peaks represent the different discharges. A 30 min resting time is considered between each discharge. A zoom on the first discharge is shown in the graphic window. The two plasma phases identified in figure 1 have the same duration as in the experiment, i.e. 2 s for the H-mode phase and 7 s for the L-mode phase.

2). Each PFC is defined by the following material layers and initial temperature $T_0(s)$ which are consistent with the JET ones:

- The first-wall PFCs are made of massive Be, with $T_0(s) = 200$ °C.
- The inner and outer divertor tiles are made of a thick layer of CFC with on top of it a W-coating layer of 15 μm, with $T_0(s) = 50 - 70$ °C.
- The different stacks of tile 5 are made of massive W, with $T_0(s) = 50$ °C.

The choice of material thicknesses and of initial temperatures are detailed in Appendix D.

Parameters for MHIMS:
After two campaigns, JET-ILW exhibits a complex pattern of surface materials: massive W, W-coating, massive Be, etc [22]. As a consequence, defining the distribution of materials for MHIMS is a difficult task to achieve. Additionally, no complete Reaction-Diffusion equations-based model exists for the HI–Be interaction at the temperature of the Be first-wall in JET-ILW, which operates around 200 °C / 473 K. Two models are however available in the literature for HI implantation at room temperature: a model including the interaction of HI with increased Be surface specific area [23], and a model that includes Be hydride formation [24]. Both aim to describe the low-temperature desorption peak observed in thermo-desorption analysis after room temperature implantation. But at a temperature of implantation in the range of the Be first-wall in JET-ILW, the HI–Be interaction behaves differently. Indeed, Reinelt et al. have reported different desorption spectra after implantation at 47 °C and at 257 °C. At the later temperature, no low-temperature peak is observed anymore while desorption peaks at higher temperature emerge. These results are consistent with reports by Anderl et al. [25]. As a consequence, we are left with no model for Be at the temperature of the ILW, and we opted for a simplified approach that considers a full massive W wall configuration. The free-parameters of the MHIMS equations for D-W interaction are given in Appendix E. A W with three kinds of traps labelled 1, 2 and 3 is considered, characterised by detrapping energies of 0.85 eV, 1.00 eV and 1.50 eV, respectively. They are supposed to model *(i)* intrinsic defects like dislocations or iron impurities, *(ii)* grain boundaries, and *(iii)* ion-induced defect like vacancies, respectively. Detrapping energies and trap densities were determine by fitting of thermal desorption spectrometry made by Ogorodnikova et al. [26]. Two sets of trap distribution were used to model massive W in MHIMS: one in the divertor

region and one in the first-wall region (cf. figure 2). The difference between the sets lies in the definition of the plasma-induced trap 3 to account for different plasma-wall interactions in the two regions. The traps profiles are presented in detail in Appendix E.

To summarise, it must be noticed that all the parameters related to the wall materials in SolEdge-EIRENE and in the thermal model WE-temp are consistent with JET-ILW materials. This applies respectively to the calculation of the reflection coefficient and of the wall temperature. It follows that not only the implantation conditions but also the thermal dynamics of the wall are consistent with JET-ILW. Only the input parameters considered for MHIMS are not consistent with the JET-ILW materials since they only consider tungsten.

5.2 Temperature dynamics.

The time evolution of the mean and maximum surface temperatures for each zone of the JET wall defined in figure 2 are displayed in figure 7 for each of the four discharges. The temperature evolution during a discharge is reproducible starting from the second discharge. This indicates that an equilibrium has been reached between the energy accumulated by the tiles during the discharge and the energy evacuated between discharges into the tokamak structure.
The evolution of the surface temperature in the divertor zones presents an increase during the H-mode phase as the result of the strong heat flux it receives. It is followed by a decrease during the L-mode phase due to the drop of the heat flux densities when the plasma detaches from both divertor targets. The heat accumulated at the surface of the material during the H-mode is conducted in the depth of the material during the L-mode phase, thus cooling down the surface. The two divertor zones hosting the strike-points undergo the strongest temperature excursions during the discharges, reaching 520 °C in the tile 5 stack C (outer strike-point) and 358 °C in the tile 3 (inner strike-point) at the end of the H-mode phase of the fourth discharge (cf. figure 7.b). During the L-mode phase, the maximum temperatures decrease up to $\sim$ 167 °C at the outer strike-point and up to 207 °C at the inner strike-point. The mean temperature of each zones of the divertor exhibits little increase during the H-mode. This indicates that the majority of the divertor remains at the initial temperature and that the temperature increase is limited to the strike-points vicinity.
Concerning the first-wall, it exhibits very limited temperature increases during the discharge, reaching a maximum of $\sim$ 208 °C at the end of the fourth discharge (cf. figure 7.d). The maximum temperature increases during both plasma phases. This increase is linear during the L-mode phase (for $t > 2$ s), which is characteristic of inertial PFCs.

5.3 Retention dynamics.

Traps 1, 2 and 3 exhibit different retention dynamics depending on their location on the wall as the implantation conditions and the wall temperature vary. These dynamics affect the D wall inventory $N_{\mathrm{wall},i}$ [D] hosted by these traps. $N_{\mathrm{wall},i}$ is obtained by spatial integration of the density of trapped particle $n_{\mathrm{t},i}$ along the material depth x, the curvilinear coordinate s and the toroidal direction (assuming toroidal symmetry). $N_{\mathrm{wall},i}$ dominates the total wall inventory as the inventory of mobile D is several orders of magnitude lower.
Figure 8 displays the time evolution of N_{wall} for the traps that present a retention dynamics at the transition from H-mode to L-mode, i.e. trap 1 in the divertor region (cf. figure 8.a) and traps 1 and 2 in the first-wall region (cf. figure 8.b). The other traps with higher detrapping energies have their inventory continuously increasing during the whole discharge, without impact of the H-L transition. Such inventory increase is characteristic of D diffusion and filling of traps in the bulk material (cf. reference [7]). The difference of behaviour of the traps between the two regions is due to their different initial wall temperature. In figure 8.a, $N_{\mathrm{wall},1}$ in the divertor is plotted in light-blue and increases during all the discharge, without any clear impact of the H-L transition. However, if we look at the contribution of the different zones of the divertor defined in figure 2 and plotted in red, we see

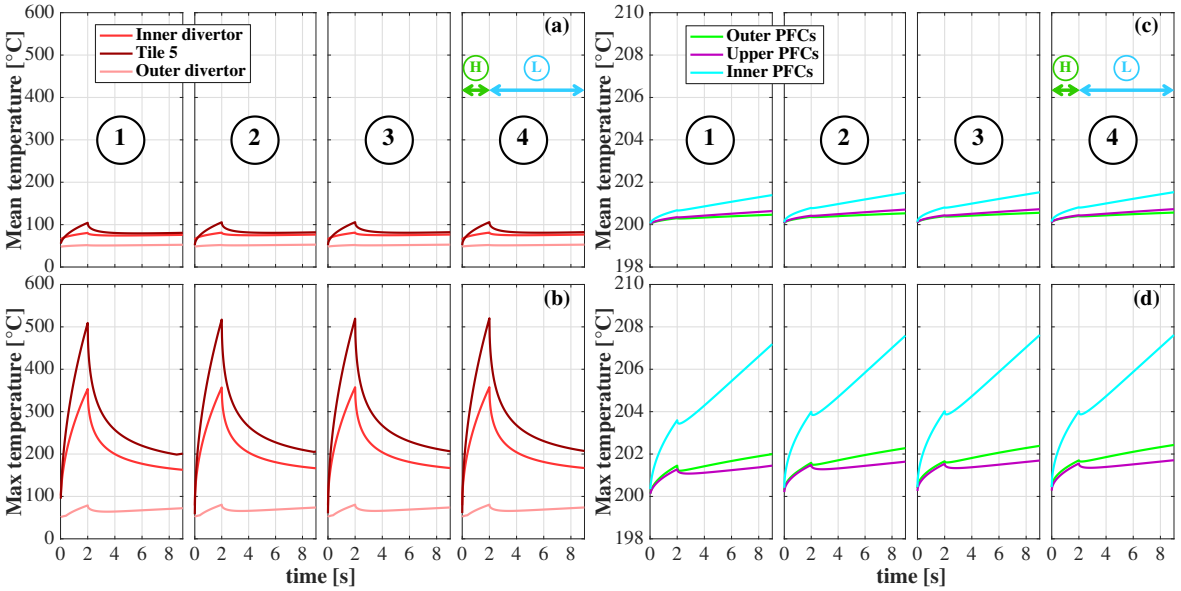

Figure 7: Time evolution of the mean and maximum PFC surface temperatures in the divertor zones ((a) and (b) respectively), and in the first-wall zones ((c) and (d) respectively) calculated by the thermal model WE-temp during each of the four plasma discharges (indicated by their number). The considered zones of the JET wall are displayed in figure 2. The H-mode phase occurs for 0 s $\leq t \leq$ 2 s while the L-mode phase occurs for 2 s $< t \leq$ 9 s.

that, in the zones hosting the strike-points (inner divertor and tile 5), the inventory increases at the beginning of the discharges and drops during the H-mode phase (from $t = 0$ s to $t = 2$ s), and then it increases again during the L-mode phase. However, these retention dynamics are very local and are not observable on $N_{\text{wall},1}$ in the whole divertor region. This decrease is more visible in discharges 1 and 2 as, for the following discharges, its amplitude is much lower than the total retention of the considered zone of the divertor.

In figure 8.b, N_{wall} in traps 1 and 2 in the first-wall region is plotted in dark blue. A sharp decrease of their inventory is observed at the H-L transition during all four discharges. The loss of D reaches 25 % of the inventory during the fourth discharge. Those detrapped D mainly refuel the plasma via outgassing. However the amplitude of this outgassing ($\sim 0.3 \times 10^{20}$ D) is very negligible w.r.t. the plasma D content ($\sim 7 \times 10^{20}$ D^+ in the zone simulated with SolEdge-EIRENE, which does not account for the plasma core): no strong impact of this outgassing is foreseen on the plasma discharge. The contribution of the different zones of the first-wall defined in figure 2 is also plotted in figure 8.b. The drop of the inventory occurs in all zones of the first-wall.

Figure 9 displays the variation in areal inventory $Inv_{\text{t},i}$ [D.m^{-2}] of trap 1, trap 2 and trap 3 between $t = 2$ s (end of H-mode phase) and $t = 9$ s (end of L-mode phase) versus the s coordinate for the fourth plasma discharge. $Inv_{\text{t},i}$ is obtained by integration of $n_{\text{t},i}$ along the material depth x. A negative variation of $Inv_{\text{t},i}$ indicates that trap i has emptied in the considered time period while a positive variation indicates a filling of trap i. In the divertor, $Inv_{\text{t},i}$ of the three traps increases everywhere, which results in the increase of the inventories observed in figure 8 during the L-mode phase. In the first-wall, the areal inventory of trap 3 increases between the two selected times. On the contrary, the traps 1 and 2 exhibit a depletion of their areal inventory. The black ellipses in figure 9.a-b indicate the locations where such depletion occur. These drops of $Inv_{\text{t},i}$ of traps 1 and 2 result in an overall decrease of the inventory of these traps in the first-wall zones as it was observed in figure 8.b.

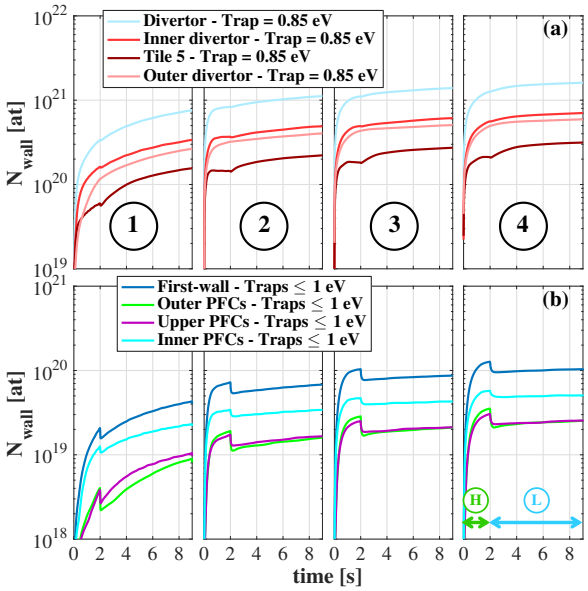

Figure 8: Time evolution of the D wall inventory N_{wall} of the trap 1 in the divertor (with $E_{\text{dt},1} = 0.85$ eV) (a) and of the traps 1 and 2 in the first-wall (with $E_{\text{dt},1} = 0.85$ eV and $E_{\text{dt},2} = 1.00$ eV) (b) during each of the four plasma discharges (indicated by their number). The inventories are also differentiated according to their location on the JET wall (cf. the different zones of the JET wall defined in figure 2).

6 Analysis of the retention dynamics during discharge n°4.

To understand the retention dynamics observed in section 5.3, an analytical model of hydrogen inventory saturation in the subsurface (several micrometers depth) under plasma implantation will be applied to the simulation. This model will be shortly introduced in the following.

6.1 Analytical model of hydrogen inventory saturation.

The analytical model has been described in reference [27] and was compared to non-linear Reaction-Diffusion simulations of D implantation in W at three different material temperatures. A good agreement was observed between the profiles of mobile/interstitial deuterium and trapped deuterium at the subsurface given by the analytical model and by the Reaction-Diffusion simulations for the three considered temperatures. Even though this model considers simplifying assumptions (steady-state, point sources for implantation, etc.), the maximum error on n_{m} and on $n_{\text{t},i}$ is of 5% in the subsurface region. Moreover, in the same reference, it was demonstrated using the analytical model that the hydrogen isotopes subsurface inventory is dominated by trapped hydrogen for tungsten in all the range of material temperature found in fusion devices.
It results that, using the analytical model, the subsurface density profiles of trapped hydrogen in the trap i, $n_{\text{t},i}^{\text{BULK}}(x)$, is expressed as function of the trap density profile, $n_i(x)$, and of a parameter called

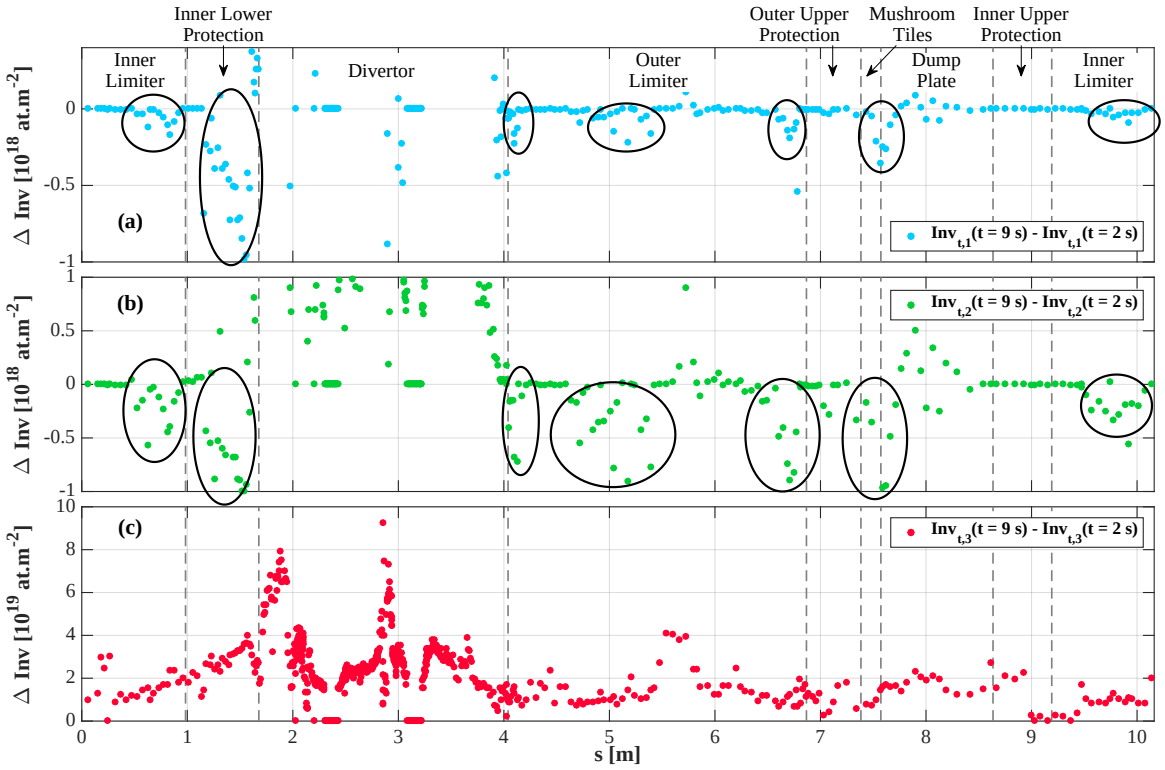

Figure 9: Distribution along the JET wall of the variation of the areal inventories $Inv_{\mathrm{t},i}$ of trap 1 (a), trap 2 (b) and trap 3 (c) between $t = 2$ s (end of H-mode phase) and $t = 9$ s (end of L-mode phase) for the fourth plasma discharge. The black ellipses indicate locations where the areal inventory of traps decreases between the end of the H-mode phase and the end of the L-mode phase.

the bulk filling ratio of the trap at steady-state, $f_{\mathrm{stat},i}^{\mathrm{BULK}}$, as follows: $n_{\mathrm{t},i}^{\mathrm{BULK}}(x) = f_{\mathrm{stat},i}^{\mathrm{BULK}} n_i(x)$, with:

$$\begin{aligned} f_{\mathrm{stat},i}^{\mathrm{BULK}} &= \frac{n_{\mathrm{t},i}^{\mathrm{BULK}}(x)}{n_i(x)} = \frac{1}{1 + \dfrac{\nu_{\mathrm{dt},i}(T)}{\nu_{\mathrm{t},i}^{*}(T)} \dfrac{n_{\mathrm{IS}}}{n_{\mathrm{m}}^{\mathrm{BULK}}}} \\ f_{\mathrm{stat},i}^{\mathrm{BULK}} &= \frac{1}{1 + \dfrac{\nu_{\mathrm{dt},i}(T)}{\nu_{\mathrm{t},i}^{*}(T)} \dfrac{n_{\mathrm{IS}} D(T)}{\Gamma_{\mathrm{imp}}^{\mathrm{i+}} X_{\mathrm{imp}}^{\mathrm{i+}} + \Gamma_{\mathrm{imp}}^{\mathrm{at}} X_{\mathrm{imp}}^{\mathrm{at}}}} \end{aligned} \tag{7}$$

where $n_{\mathrm{m}}^{\mathrm{BULK}}$ defines the value of the density of mobile extending in the bulk direction (flat profile up to several micrometers). $X_{\mathrm{imp}}^{\mathrm{i+}}$ and $X_{\mathrm{imp}}^{\mathrm{at}}$ are the mean implantation depths of ions and atoms respectively [m]. The expression of $f_{\mathrm{stat},i}^{\mathrm{BULK}}$ is simplified assuming that only diffusion limits trapping, which implies $\nu_{\mathrm{t},i}^{*}(T) = D(T)/\lambda^2$ with λ the distance between two interstitial sites for HI, as in the DWE simulation shown in this article (cf. Appendix E):

$$\begin{aligned} f_{\mathrm{stat},i}^{\mathrm{BULK}} &= \frac{1}{1 + \dfrac{\nu_{\mathrm{dt},i}(T) \lambda^2 n_{\mathrm{IS}}}{\Gamma_{\mathrm{imp}}^{\mathrm{i+}} X_{\mathrm{imp}}^{\mathrm{i+}} + \Gamma_{\mathrm{imp}}^{\mathrm{at}} X_{\mathrm{imp}}^{\mathrm{at}}}} \\ f_{\mathrm{stat},i}^{\mathrm{BULK}} &= \frac{1}{1 + \dfrac{\nu_{\mathrm{dt},i}(T)}{\nu_{\mathrm{t}}^{\mathrm{BULK}}(\Gamma_{\mathrm{imp}}^{\mathrm{i+}}, X_{\mathrm{imp}}^{\mathrm{i+}}, \Gamma_{\mathrm{imp}}^{\mathrm{at}}, X_{\mathrm{imp}}^{\mathrm{at}})}} \end{aligned} \tag{8}$$

This expression allows to determine if trap i is filled or empty. $f_{\mathrm{stat},i}^{\mathrm{BULK}}$ presents a ratio between the detrapping frequency from trap i ($\nu_{\mathrm{dt},i}$), which only depends on the material temperature, and $\nu_{\mathrm{t}}^{\mathrm{BULK}}$ or maximum bulk trapping frequency, which only depends on the implantation conditions (flux densities and mean implantation ranges). The comparison between $\nu_{\mathrm{dt},i}$ and $\nu_{\mathrm{t}}^{\mathrm{BULK}}$ enables to highlight the process that dominates the interaction between HI and traps:

- when $\nu_{\mathrm{dt},i} \gg \nu_{\mathrm{t}}^{\mathrm{BULK}}$, detrapping is more efficient than trapping, $f_{\mathrm{stat},i}^{\mathrm{BULK}}$ tends to 0 and the trap i remains empty.
- when $\nu_{\mathrm{dt},i} = \nu_{\mathrm{t}}^{\mathrm{BULK}}$, $f_{\mathrm{stat},i}^{\mathrm{BULK}}$ is equal to 0.5 and the trap i is half filled with HI.
- when $\nu_{\mathrm{dt},i} \ll \nu_{\mathrm{t}}^{\mathrm{BULK}}$, trapping is more efficient than detrapping, $f_{\mathrm{stat},i}^{\mathrm{BULK}}$ tends to 1 and the trap i saturates.

6.2 Analysis of the discharge.

6.2.1 $f_{\mathrm{stat},i}^{\mathrm{BULK}}$.

The parameter $f_{\mathrm{stat},i}^{\mathrm{BULK}}$ is now used to provide a more detailed analysis of the wall inventory during the fourth discharge, enabling the understanding of the retention dynamics shown in figure 8. The distribution along the JET wall of $f_{\mathrm{stat},i}^{\mathrm{BULK}}$ is plotted for trap 1, trap 2 and trap 3 in figure 10. The value of $f_{\mathrm{stat},i}^{\mathrm{BULK}}$ are calculated at $t = 2$ s (end of H-mode phase) and $t = 9$ s (end of L-mode phase) for the fourth plasma discharge. $f_{\mathrm{stat},i}^{\mathrm{BULK}}$ is calculated using equation 7 for each cell on the wall, considering the surface temperature calculated by WE-temp, the implantation flux density of ions and atoms provided by EIRENE and the mean implantation ranges of ions and atoms given by SRIM tables. One can note the following

- Divertor, strike-points vicinity: for trap 1 and trap 2, $f_{\mathrm{stat},i}^{\mathrm{BULK}}$ is higher at the end of the H-mode than at the end of the L-mode (orange ellipses in figure 10.a-b). This results in the increase of the inventory in the zones hosting the strike-points which was previously observed for trap 1 in figure 8.a. For trap 3, $f_{\mathrm{stat},3}^{\mathrm{BULK}} = 1$ and this trap saturates. One can notice a little increase of $f_{\mathrm{stat},3}^{\mathrm{BULK}}$ at the outer strike-point (cf. orange ellipse in figure 10.c).
- Divertor, away from the strike-points: the three traps are fully saturated for the two considered times, with $f_{\mathrm{stat},i}^{\mathrm{BULK}} = 1$.
- First-wall: the areas where $Inv_{\mathrm{t},1}$ and $Inv_{\mathrm{t},2}$ decrease between the two selected times (identified with black ellipses in figure 9) correspond to locations where $f_{\mathrm{stat},1}^{\mathrm{BULK}}$ and $f_{\mathrm{stat},2}^{\mathrm{BULK}}$ decrease (cf. black ellipses in figure 10). $f_{\mathrm{stat},1}^{\mathrm{BULK}}$ ranges between 0 and 0.1 in all the first-wall which means that this trap is almost empty. $f_{\mathrm{stat},2}^{\mathrm{BULK}}$ ranges from 0 to 0.8 which indicates that this trap is partly filled. Concerning trap 3, it remains saturated in the time period with $f_{\mathrm{stat},3}^{\mathrm{BULK}} = 1$ everywhere in the wall (cf. figure 10.c): the trap saturates and is filled by diffusion and trapping in the depth of W.

6.2.2 $\nu_{\mathrm{dt},i}$ vs. $\nu_{\mathrm{t}}^{\mathrm{BULK}}$.

To find out the cause for these evolutions, the evolution of both frequencies involved in the expression of $f_{\mathrm{stat},i}^{\mathrm{BULK}}$, equation 7, is analysed. In figure 11, the distribution along the JET wall of the detrapping frequency $\nu_{\mathrm{dt},i}$ for trap 1, trap 2 and trap 3 are plotted for the two considered times ($t = 2$ s and $t = 9$ s) during the fourth plasma discharge.

- Divertor, strike-points vicinity: during the H-mode, the wall temperature raises from initial temperature to ~ 350 °C at the inner strike-point and to ~ 500 °C at the outer strike-point as it was shown in section 5.2. Thus, $\nu_{\mathrm{dt},i}$ raises for the three traps as it can be seen in figures

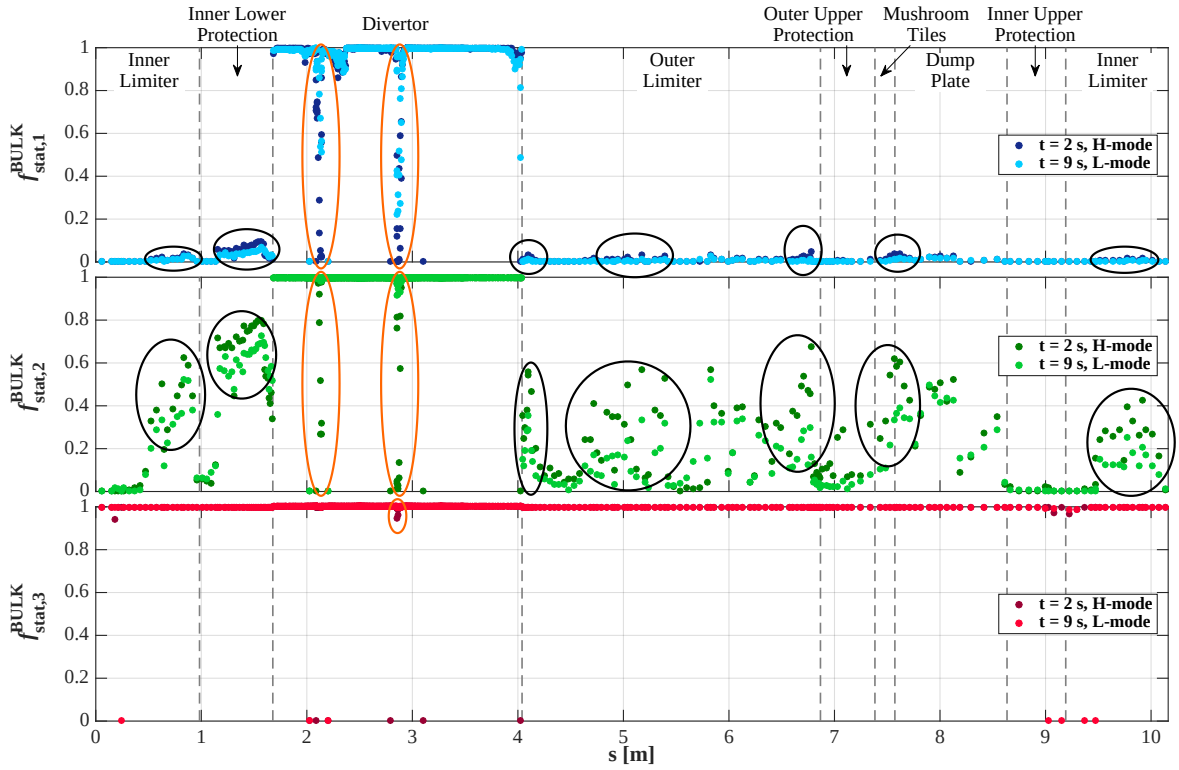

Figure 10: Distribution along the JET wall of the bulk filling ratio of traps at steady-state, $f_{\mathrm{stat},i}^{\mathrm{BULK}}$, of trap 1 (a), trap 2 (b) and trap 3 (c) calculated at $t = 2$ s (end of H-mode phase) and at $t = 9$ s (end of L-mode phase) for the fourth plasma discharge. The black ellipses indicate locations where $f_{\mathrm{stat},i}^{\mathrm{BULK}}$ decreases between the end of the H-mode phase and the end of the L-mode phase, leading to a release of D from the corresponding traps. The orange ellipses highlight two spots in the divertor (the vicinity of both strike-points) where $f_{\mathrm{stat},i}^{\mathrm{BULK}}$ increases between the two selected times, which implies a filling of traps.

11.(a-c), respectively for 2.0 m $\leq s \leq$ 2.2 m and for 2.8 m $\leq s \leq$ 3.0 m. $\nu_{\mathrm{dt},i}$ is higher at the end of the H-mode than at the end of the L-mode due to the cooling of the surface during the L-mode (cf. figure 7.b). This decrease of $\nu_{\mathrm{dt},i}$ between the two considered times is tremendous, from three orders of magnitude for trap 1 up to six orders of magnitude for trap 3 at the outer strike-point (where the highest surface temperature is found).

– Divertor, away from the strike-points: $\nu_{\mathrm{dt},i}$ does not evolve between the two times for the three traps as these areas do not exhibit strong temperature excursion during the discharge due to the low heat flux density (cf. section 5.2).

– First-wall: the first-wall stays almost at the initial temperature of 200 °C during all the discharge due to low heat flux in this region. Therefore $\nu_{\mathrm{dt},i}$ does not evolve between the two times for the three traps. One can note that $\nu_{\mathrm{dt},i}$ are higher in the first-wall than in the divertor due to the higher base temperature of the first-wall (200 °C, 50 – 70 °C for the divertor).

Then the distribution of $\nu_{\mathrm{t}}^{\mathrm{BULK}}$ along the JET wall for the two considered times is displayed in figure 12. This frequency is the same for the three traps. Everywhere in the vacuum vessel, $\nu_{\mathrm{t}}^{\mathrm{BULK}}$ decreases between the two phases, except in some shadowed region of the divertor and in the private flux region. Comparing $\nu_{\mathrm{dt},i}$ in figure 11 and $\nu_{\mathrm{t}}^{\mathrm{BULK}}$ in figure 12, the retention dynamics in traps induced by the change of plasma phases can be understood:

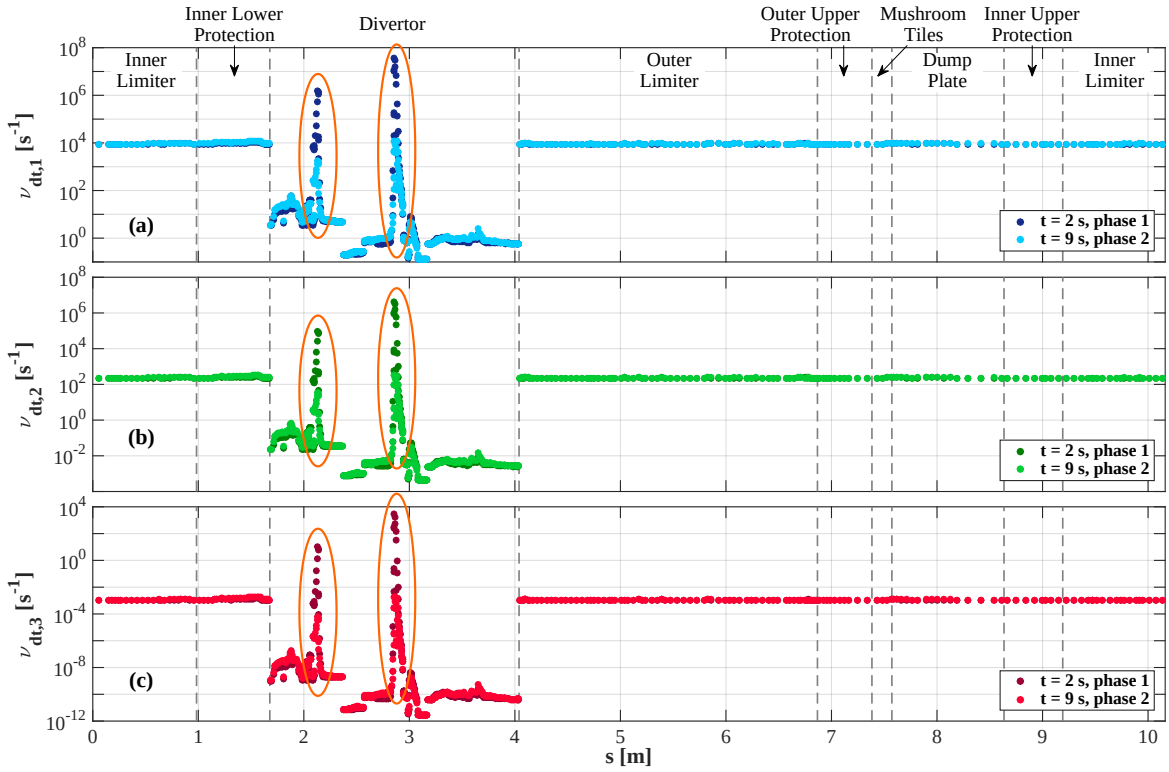

Figure 11: Distribution along the JET wall of the detrapping frequency $\nu_{\mathrm{dt},i}$ for trap 1 (a), trap 2 (b) and trap 3 (c) calculated at $t = 2$ s (end of H-mode phase) and at $t = 9$ s (end of L-mode phase) for the fourth plasma discharge.

– Divertor, strike-points vicinity: During the H-mode, at the beginning of the discharge, the temperature at the strike-points is low and traps 1 and 2 are filled with D atoms as $\nu_{\mathrm{dt},i} \ll \nu_{\mathrm{t}}^{\mathrm{BULK}}$. Then the temperature increases due to high heat flux densities, entailing the increase of $\nu_{\mathrm{dt},1}$ which becomes higher than $\nu_{\mathrm{t}}^{\mathrm{BULK}}$: trap 1 releases D as observed in figure 8.a. At the end of the H-mode, the temperature at both strike-points is high (350 °C at the inner strike-point, 500 °C at the outer strike-point), and both traps 1 and 2 tend to empty completely as $\nu_{\mathrm{dt},i} \gg \nu_{\mathrm{t}}^{\mathrm{BULK}}$ (cf. orange ellipses in figures 11a-b and 12a-b). At the same moment, the value of $\nu_{\mathrm{dt},3}$ is of same order of magnitude as $\nu_{\mathrm{t}}^{\mathrm{BULK}}$ at the outer strike-point, and $f_{\mathrm{stat},3}^{\mathrm{BULK}}$ decreases to 0.95 (cf. orange ellipse in figure 10.c): the trap 3 starts to release D. A longer H-mode would have induced higher temperatures at both strike-points and therefore a complete release of D trapped in trap 3. During the L-mode, the heat flux densities decrease strongly and the surface of the tiles hosting the strike-points is cooled by heat conduction in the depth of the tiles as observed in figure 7.b: $\nu_{\mathrm{dt},i}$ decreases for the three traps. $\nu_{\mathrm{t}}^{\mathrm{BULK}}$ also decreases by one order of magnitude at both strike-points due to the decrease of the impact energy by a factor of 8 to 32 in both tiles inducing a drop of X_{imp} of both ions and atoms. For trap 2 and trap 3, the detrapping frequency is 1 to 6 orders of magnitude lower than $\nu_{\mathrm{t}}^{\mathrm{BULK}}$ at the end of the L-mode: $f_{\mathrm{stat},2}^{\mathrm{BULK}}$ and $f_{\mathrm{stat},3}^{\mathrm{BULK}}$ are equal to 1. The trap 2, which was empty in the vicinity of both strike-points at the end of the H-mode phase, got completely refilled during the L-mode phase leading to a pumping of D. For trap 1, $\nu_{\mathrm{dt},1}$ is of same order of magnitude as $\nu_{\mathrm{t}}^{\mathrm{BULK}}$ at both strike-points. Its filling ratio increases from 0 at the end of the H-mode up to 0.5 and 0.2 at the inner and outer strike-points respectively at the end of the L-mode: the trap 1 pumps D during the L-mode phase as observed in figure 8.a.

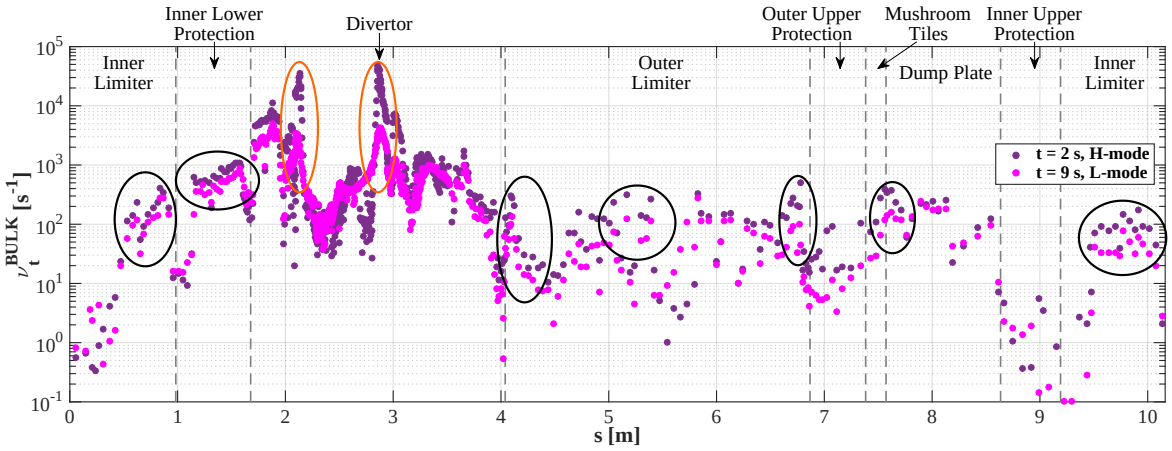

Figure 12: Distribution along the JET wall of the bulk trapping frequency ν_t^{BULK} calculated at $t = 2$ s (end of H-mode phase) and at $t = 9$ s (end of L-mode phase) for the fourth plasma discharge. This characteristic frequency is similar for the three traps and only depends on the implantation conditions. The expression of ν_t^{BULK} is reported in equation 7. The black ellipses indicate locations, identified in figure 9, where the areal inventory of trap 1 and trap 2 has decreased between the end of H-mode phase and the end of the L-mode phase, leading to a release of D from the corresponding traps. The orange ellipses highlight two spots in the divertor (the vicinity of both strike-points) where $f_{stat,i}^{BULK}$ increases between the two selected times as indicated in figure 11.

- Divertor, away from the strike-points: for the three traps, $\nu_{dt,i}$ is two to fourteen orders of magnitude below ν_t^{BULK}. $f_{stat,i}^{BULK}$ is equal to 1 for the two phases even though the implantation conditions evolve (leading to a decrease of ν_t^{BULK}): the three traps remains saturated and the wall keeps on pumping D from the plasma through diffusion of D in the depth of the material and filling of the traps.

- First-wall: for the three traps, $\nu_{dt,i}$ remains constant during the two phases as the temperature variation is moderate during the discharge. On the contrary, ν_t^{BULK} evolves in all the first-wall between the two phases. For trap 1 and trap 2, ν_t^{BULK} is of the same order of magnitude as $\nu_{dt,1}$ and $\nu_{dt,2}$ in most of the first-wall (10^1 – 10^4 s^{-1}). In the areas indicated with black ellipses in figure 12, a decrease of ν_t^{BULK} between the two phases is noted, which entails the decrease of $f_{stat,1}^{BULK}$ and $f_{stat,2}^{BULK}$ that has been observed in figure 10a-b. The inventory in those two traps drops between the two phases due the change of implantation conditions. It was seen in section 3 that the mean implantation flux density in the three zones remains almost constant between the two phases (with variation by a factor of 0.81 to 1.3 depending on the zone). Thus, the drop of ν_t^{BULK} is attributed to the decrease of the impact energy of both ions and atoms between the two phases (by a factor of 1.8 to 2.8) which entails a decrease of their mean implantation range. For trap 3, the drop of ν_t^{BULK} has no impact as $\nu_{dt,3}$ is three to six orders of magnitude lower than ν_t^{BULK}: $f_{stat,3}^{BULK}$ is equal to 1 during the two phases and the trap remains saturated.

6.3 Main conclusion.

To summarise, the retention dynamics observed in traps at the transition from H-mode to L-mode during the DWE simulation of full-W JET discharges were explained by the analytical model based on the filling ratio of traps $f_{stat,i}^{BULK}$. The following retention dynamics are pointed out:

(i) The retention dynamics resulting from variation of temperature for constant implantation conditions are summed up in table 5.1.

At constant implantation conditions	$\nearrow T$	$\searrow T$
Detrapping frequency $\nu_{\mathrm{dt},i}(T)$ [s^{-1}]	$\nearrow$	$\searrow$
Filling ratio of traps $f_{\mathrm{stat},i}^{\mathrm{BULK}}$	$\searrow$	$\nearrow$
Traps areal inventory $Inv_{\mathrm{t},i}$ [$\mathrm{HI.m}^{-2}$]	$\searrow$	$\nearrow$
Retention dynamics	Fuelling	Pumping

Table 5.1: Retention dynamics as a function of temperature for constant implantation conditions (implantation flux densities, impact energy and angle of incidence). This table applies to materials for which the hydrogen recombination at the surface is not the rate-limiting step.

The fuelling effect at constant implantation conditions is observed in the DWE simulation in the vicinity of both strike-points during the H-mode phase: the high surface temperature reached at the end of this phase leads to a detrapping of D from traps with low detrapping energy. This explains the decrease of the trap 1 inventory observed at the end of the H-mode phase. During the L-mode phase, the decrease of the surface temperature at both strike-points leads to decrease of the detrapping frequency of this trap resulting in an increase of the local inventory and therefore a pumping effect from the plasma point of view.

(ii) The retention dynamics resulting from variation of implantation conditions at fixed temperature are summed up in table 5.2.

At constant temperature	$\nearrow (\Gamma_{\mathrm{imp}}^{\mathrm{i+}} X_{\mathrm{imp}}^{\mathrm{i+}} + \Gamma_{\mathrm{imp}}^{\mathrm{at}} X_{\mathrm{imp}}^{\mathrm{at}})$	$\searrow (\Gamma_{\mathrm{imp}}^{\mathrm{i+}} X_{\mathrm{imp}}^{\mathrm{i+}} + \Gamma_{\mathrm{imp}}^{\mathrm{at}} X_{\mathrm{imp}}^{\mathrm{at}})$
Max trapping frequency $\nu_{\mathrm{t}}^{\mathrm{BULK}}$ [s^{-1}]	$\nearrow$	$\searrow$
Filling ratio of traps $f_{\mathrm{stat},i}^{\mathrm{BULK}}$	$\nearrow$	$\searrow$
Traps areal inventory $Inv_{\mathrm{t},i}$ [$\mathrm{HI.m}^{-2}$]	$\nearrow$	$\searrow$
Retention dynamics	Pumping	Fuelling

Table 5.2: Retention dynamics as a function of implantation conditions for constant surface temperature. This table applies to materials for which the hydrogen recombination at the surface is not the rate-limiting step.

Such retention dynamics is also observed in the DWE simulation in the first-wall. A release of D is observed after the transition from the H-mode phase to the L-mode phase while the first-wall temperature variation remains moderate during all the discharge. This release of D is attributed to the decrease of the impact energy of both ions and atoms between the two phases (by a factor of 1.8 to 2.8) which entails a decrease of their mean implantation range and consequently a decrease of the stationary filling ratio of traps $f_{\mathrm{stat},i}^{\mathrm{BULK}}$.

7 Discussions.

Tables 5.1 and 5.2 are consistent with the retention dynamics observed in tokamaks and mentioned in the introduction. The transient release of particle from the outer divertor plate observed in JT-60U during long and high-power-heated discharges [4] is due to the temperature increase in the vicinity of the strike-points due to the strong plasma heat flux. This temperature increase leads to an increase of the detrapping frequency of the traps. According to table 5.1, the traps inventory depletes leading to a fuelling of the plasma. This transient release is also observed in the simulation presented in this article at the vicinity of both strike-points for the trap 1 with low detrapping energy. This detrapping occurs at a relatively low temperature ($\sim$ 500 K). However, this phenomenon is observed at a higher

temperature of $\sim$ 900 K in JT-60U as hydrogen is know to desorb at higher temperature in C [28, 29] than in W [11, 26].
On the contrary, the transient release of D observed in JET-ILW at the transition between the H-mode and the L-mode phases during high-density H-mode discharges [2] cannot be attributed to material heating as the input power decreases between these two phases. Table 5.2 could explain this fuelling effect by a decrease of the product between the implantation flux density and the mean implantation range of ions and atoms. This phenomenon also occurs in the simulation at the transition from H-mode to L-mode in the low energy traps of the first-wall and has been attributed to the decrease of the impact energy of both ions and atoms between the two phases. Such decrease of the impact energy could be responsible for the experimental release of particles in JET-ILW as the power injected into the plasma strongly decreases due to the NBI power cut-off.
However, the amplitude of the D release in the simulation ($\sim 0.003 \times 10^{22}$ D in figure 8.b) is way below the one experimentally observed[1] ($\sim 9.0 \times 10^{22}$ D). This is due to the low detrapping energy of the traps involved in the dynamics observed in the simulation (trap 1 with $E_{\mathrm{dt},1} = 0.85$ eV and trap 2 with $E_{\mathrm{dt},2} = 1.0$ eV) which entails almost empty traps in the first-wall during both phases. Also these traps cannot store such amount of D due to their very low trap densities (≤ 0.1 at.%). Even the trap 3, with $E_{\mathrm{dt},3} = 1.5$ eV and a trap density of 15 at.% in the implantation zone, does not retain sufficient D in the first-wall ($\sim 4.0 \times 10^{22}$ D at the end of the fourth discharge). This indicates that the JET-ILW first-wall may have traps with detrapping energy between 1.0 eV and 1.5 eV, and with a higher density in the implantation zone. Beryllium may contain such traps as:

(i) it is known to store hydrogen up to a concentration of $\sim$ 30 at.% in the implantation zone [8], i.e. a density four times higher than the one considered in the simulation.

(ii) almost 75 % of this inventory desorbs at low temperature (between 400 and 500 K) as observed in thermo-desorption spectrometry of hydrogen-implanted beryllium [10, 11, 12]. This low-temperature desorption peak has recently been qualitatively reproduced by a desorption model of hydrogen adsorbed at the beryllium surface, with recombination activation energy of 1.0 eV [23].

Please note that the dynamics observed in the simulation would not have been modified by such kind of traps. Indeed, the parameter $f_{\mathrm{stat},i}^{\mathrm{BULK}}$ does not depend on the trap density (cf. equation 7). As a consequence, the trap retention dynamics (pumping or fuelling of D) observed in the simulation are independent of the trap density. However, the amplitude of these dynamics as well as their kinetic strongly depend on that density. Only simulations with DWE can give an idea of both amplitude and rate of these dynamics.

8 Conclusions.

The Dynamics of Wall Elements (DWE) code is able to simulate the hydrogen isotopes retention at the scale of fusion devices, during and between discharges. The architecture of DWE has been introduced as well as its interaction with the SolEdge-EIRENE code, which provides the implantation quantities to DWE along the device wall. DWE is composed of two internal codes: *(i)* WE-temp, which determines the wall temperature, and *(ii)* MHIMS, which determine the transport, trapping and desorption of hydrogen isotopes in the wall material.
In this work, four consecutive pure deuterium discharges are modeled and analysed with DWE. These discharges are identical and present a transition from a H-mode phase to a L-mode phase, which induces strongly different plasma-wall interactions. A 30 min resting time (without plasma) was also simulated between each discharge. Each phase of the discharge was simulated with SolEdge-EIRENE, providing the implantation quantities as fixed inputs to DWE during the duration of each phase. Due to the

[1] The amplitude of the D release experimentally observed in the JET-ILW in reference [2] may be overestimated by the underestimation of the effective pumping speed of the divertor cryopump which is know to be pressure-dependent.

lack of suitable retention model and parameters for deuterium-beryllium interaction, this simulation has been performed in the JET tokamak considering a full tungsten wall.
For the thermal dynamics, the temperature evolution is similar from the second discharge which indicates that an equilibrium has been reached between the energy accumulated by the tiles during the discharge and the energy evacuated between discharges. The highest temperatures are found in both strike-points during the H-mode phase (350 °C at the inner strike-point, 500 °C at the outer strike-point), where high heat fluxes are deposited. During the L-mode phase, the plasma is detached, the heat flux is lower at both strike-points and the wall temperature strongly decreases by heat conduction in the PFC depth. The first-wall and the remote areas of the divertor remain at their base temperature (200 °C and 50 – 70 °C respectively) during all the discharge due to the low heat flux density to which they are exposed.
The simulation reveals retention dynamics in traps with low detrapping energy. These dynamics were explained by a simple parameter, the bulk filling ratio of the trap at steady-state, $f_{\mathrm{stat},i}^{\mathrm{BULK}}$, which was introduced in reference [27]. $f_{\mathrm{stat},i}^{\mathrm{BULK}}$ presents a ratio between the detrapping frequency from trap i ($\nu_{\mathrm{dt},i}$), which only depends on the material temperature, and $\nu_{\mathrm{t}}^{\mathrm{BULK}}$ or maximum bulk trapping frequency, which only depends on the implantation conditions (flux densities and mean implantation ranges). The comparison between $\nu_{\mathrm{dt},i}$ and $\nu_{\mathrm{t}}^{\mathrm{BULK}}$ enables to highlight the process that dominates the interaction between deuterium and traps (trapping or detrapping). The retention dynamics observed in the simulation are the following. *(i)* First, a release of deuterium is observed at the vicinity of both strike-points at the end of the H-mode phase. This dynamics is explained by an increase of the wall temperature at both strike-points, leading to an increase of $\nu_{\mathrm{dt},i}$ during this phase: detrapping from trap with low detrapping energy becomes more favourable than trapping and this trap releases deuterium. On the contrary, during the subsequent L-mode phase, the wall temperature at the strike-points decreases, $\nu_{\mathrm{dt},i}$ decreases leading to retention by filling of this trap. Such transient release of deuterium has been observed in JT-60U with a carbon wall during long and high-power-heated discharges [4]. However, it occurred at a higher temperature of $\sim$ 900 K in JT-60U as deuterium is know to desorb at higher temperature in carbon. *(ii)* Secondly, a release of deuterium from the first-wall is observed at the transition between the H-mode and the L-mode. Such dynamics cannot be attributed to change of wall temperature as the first-wall remains at its base temperature (200 °C) during the whole discharge and $\nu_{\mathrm{dt},i}$ remains constant. This dynamics has been attributed to a decrease of the implantation energy of deuterium between the two phases, as it entails a shallower implantation of deuterium and therefore a decrease of $\nu_{\mathrm{t}}^{\mathrm{BULK}}$: trapping becomes less favourable than detrapping and traps with low detrapping energy release deuterium. This offers a possible explanation of the strong transient release of deuterium experimentally observed in the JET-ILW at the NBI cut-off during high density H-mode discharges [2]. The quantity of detrapped deuterium in the simulation ($\sim 0.003 \times 10^{22}$ D) is below the one experimentally observed [2]. This underestimation is attributed to the consideration of tungsten first-wall as beryllium is known to host traps with densities four times higher than the one considered in the simulation. It suggests that beryllium may be responsible for the strong dynamic retention observed in the JET-ILW

Acknowledgements

This work has been carried out within the framework of the EUROfusion Consortium, funded by the European Union via the Euratom Research and Training Programme (Grant Agreement No 101052200 – EUROfusion). Views and opinions expressed are however those of the author(s) only and do not necessarily reflect those of the European Union or the European Commission. Neither the European Union nor the European Commission can be held responsible for them.
The project leading to this publication has received funding from the Excellence Initiative of Aix-Marseille University – A*Midex, a French "Investissements d'Avenir" programme as well as from the ANR under grant ANR-18-CE05-12.
Centre de Calcul Intensif d'Aix-Marseille is acknowledged for granting access to its high performance

computing resources.

Appendix A: SolEdge-EIRENE simulations set up.

The H-mode and L-mode stationary phases of discharge #JPN89044 are modelled with the SolEdge-EIRENE edge-plasma transport code to obtain plasma backgrounds representative of the experimental ones. The simulation inputs for both phases are consistent with the experimental values. First, the cross-field transport coefficients for particle and energy are automatically set up to fit experimental reference upstream profiles of density and temperatures (taken at the JET outer mid-plane) obtained with Thomson Scattering measurements during each phase of #JPN89044. For the H-mode phase, only inter-ELM profiles are considered since the modelling of the ELM transients is not conceivable due to its computational cost. The profiles of density and temperature are also automatically shifted with respect to the magnetic separatrix in order to force the Scrape-Off Layer (SOL) input power (P_{SOL}) to match the experimental one ($P_{\mathrm{SOL}} = P_{\mathrm{in}} - P_{\mathrm{rad,core}}$ with P_{in} the input power and $P_{\mathrm{rad,core}}$ the radiative power in the plasma core. P_{SOL} is equal to 10 MW for the H-mode phase and 2.5 MW for the L-mode phas). The experimental fuelling rates and locations (cf. section 2) are respected and the NBI fuelling is considered during the H-mode phase. A Be first-wall (from $1 \rightarrow 2$ clockwise in figure 2) and a W divertor (from $2 \rightarrow 1$) are considered for particle reflection properties. A Be surface is also assumed on the top of HFGC tile and tile 1, in agreement with post-mortem analysis that revealed the presence of a thick (up to 40 μm) Be co-deposit layers in this zone of JET-ILW [30]. A molecular recycling coefficient (R_{m}, cf. reference [27]) of unity is considered everywhere in the wall (under the assumption that plasma conditions are weakly dependent on R_{m}), except in the two divertor throats (where the pumping ducts are located). A specified value is set there in order to force the pumping flux, Q_{pump}, to ensure a stationary particle balance ($Q_{\mathrm{inj}} + Q_{\mathrm{NBI}} = Q_{\mathrm{pump}}$) in the simulations.

Appendix B: General equation of WE-temp and example of calculation of a PFC temperature.

We herein demonstrate the general equation of WE-temp, equation 4. One will focus on the resolution of the Duhamel integral 1 (the PFC step response calculation will be addressed in appendix C). To solve this convolution integral, one will use the property of Laplace transform w.r.t. that type of integral. First the Laplace transform $F(p)$ of a function $f(t)$ has to be introduced:

$$\mathscr{L}\left[f(t)\right] \equiv F(p) = \int_0^{+\infty} e^{-pt} f(t) dt \tag{9}$$

where p is the Laplace transform variable (complex number). The inversion formula is:

$$\mathscr{L}^{-1}[F(p)] \equiv f(t) = \frac{1}{2\pi i} \int_{\gamma - i\cdot\infty}^{\gamma + i\cdot\infty} e^{pt} F(p) dp \tag{10}$$

where γ is a real number so that the contour path of integration is in the region of convergence of $F(p)$.
First, from equation 1, we can define the temperature variation $\Delta T_i(s,x,t)$:

$$\Delta T_i(s,x,t) = \overline{T_i}(s,x,t) - T_i(s,x,0) = \int_0^t \Phi_{\mathrm{net}}(s,\tau) \frac{\partial T_i^{\mathrm{step}}(s,x,t-\tau)}{\partial t} \, d\tau \tag{11}$$

We can then calculate the Laplace transform of ΔT_i using the properties of the Laplace transform

w.r.t. convolution and derivative of function [14]:

$$\begin{aligned}\mathscr{L}\left[\Delta T_i(s,x,t)\right] &= \mathscr{L}\left[\phi_{\text{net}}(s,t)\right]\cdot\mathscr{L}\left[\frac{\partial T_i^{\text{step}}(s,x,t)}{\partial t}\right]\\ &= \mathscr{L}\left[\phi_{\text{net}}(s,t)\right]\cdot\left(p\mathscr{L}\left[T_i^{\text{step}}(s,x,t)\right]+\cancel{T_i^{\text{step}}(s,x,0)}\right)\\ &= \mathscr{L}\left[\phi_{\text{net}}(s,t)\right]\cdot p\mathscr{L}\left[T_i^{\text{step}}(s,x,t)\right]\end{aligned} \tag{12}$$

where the initial condition 2e has been accounted.
The Laplace transform of Φ_{net}, defined in equation 3, can easily be obtained from Laplace transform table [14]:

$$\begin{aligned}\mathscr{L}\left[\Phi_{\text{net}}(s,t)\right] &= \sum_{k=1}^{N_\phi(s,t)}\Delta\phi_k(s)\mathscr{L}\left[\mathcal{H}(s,t-t_k(s))\right]\\ &= \sum_{k=1}^{N_\phi(s,t)}\Delta\phi_k(s)\frac{e^{-t_k p}}{p}\end{aligned} \tag{13}$$

Equation 13 can be introduced in equation 12:

$$\begin{aligned}\mathscr{L}\left[\Delta T_i(s,x,t)\right] &= \left(\sum_{k=1}^{N_\phi(s,t)}\Delta\phi_k(s)\frac{e^{-t_k p}}{p}\right)\cdot p\mathscr{L}\left[T_i^{\text{step}}(s,x,t)\right]\\ &= \sum_{k=1}^{N_\phi(s,t)}\left(\Delta\phi_k(s)e^{-t_k p}\mathscr{L}\left[T_i^{\text{step}}(s,x,t)\right]\right)\end{aligned} \tag{14}$$

ΔT_i can be obtained by inverting equation 14 using table of inversion [14]:

$$\begin{aligned}\Delta T_i(s,x,t) &= \mathscr{L}^{-1}\left\{\sum_{k=1}^{N_\phi(s,t)}\left(\Delta\phi_k(s)e^{-t_k p}\mathscr{L}\left[T_i^{\text{step}}(s,x,t)\right]\right)\right\}\\ &= \sum_{k=1}^{N_\phi(s,t)}\left(\Delta\phi_k(s)\mathscr{L}^{-1}\left\{e^{-t_k p}\mathscr{L}\left[T_i^{\text{step}}(s,x,t)\right]\right\}\right)\\ &= \sum_{k=1}^{N_\phi(s,t)}\Delta\phi_k(s)T_i^{\text{step}}(s,x,t-t_k(s))\end{aligned} \tag{15}$$

Equation 15 can be inserted in equation 11 to recover WE-temp equation 4a.

To illustrate the calculation of the temperature using equation 4, an actively-cooled ITER-like monoblock made of three material layers is considered (cf. figure 5). The PFC material specifications are shown in table 9. The different layers are assumed to be in perfect contact ($R_{c_i}=0$). The considered heat convection coefficient is $h = 36352$ W.m^{-2}.°C^{-1} [13].
This PFC is submitted to a uniform net heat flux density ϕ_{net} displayed in figure 13.a in black solid line. Due to its uniformity, ϕ_{net} is not function of s, and the s coordinate will be omitted in the following. ϕ_{net} can be decomposed in three step changes (cf. figure 13.a): $\Delta\phi_1 = +2$ MW.m^{-2} at $t_1 = 1$ s (red area), $\Delta\phi_2 = +1$ MW.m^{-2} at $t_2 = 3$ s (green area) and $\Delta\phi_3 = -0.5$ MW.m^{-2} at $t_3 = 4$ s (blue area). According to equation 15, the surface temperature variation, $\Delta T_1(0,t)$, is equal to the sum of the surface temperature variations $\Delta T_1^1(0,t)$, $\Delta T_1^2(0,t)$ and $\Delta T_1^3(0,t)$ respectively due to the three step changes $\Delta\phi_1$, $\Delta\phi_2$ and $\Delta\phi_3$:

$$\begin{aligned}\Delta T_1(0,t) &= \Delta T_1^1(0,t) + \Delta T_1^2(0,t) + \Delta T_1^3(0,t)\\ \Delta T_1(0,t) &= \Delta\phi_1 T_1^{\text{step}}(0,t-t_1) + \Delta\phi_2 T_1^{\text{step}}(0,t-t_2) + \Delta\phi_3 T_1^{\text{step}}(0,t-t_3)\end{aligned} \tag{16}$$

Layer number	Material	Thickness e_i (mm)	λ_i (W.m^{-1}.°C^{-1})	c_{p_i} (J.kg^{-1}.°C^{-1})	ρ_i (kg.m^{-3})
1	W	11	165	132	19279
2	Cu OFHC	1	377	387	8720
3	CuCrZr	1.5	320	376	376

Table 9: Technical specifications of the PFC considered in the example of surface temperature calculation. The material thermal properties are taken at 100 °C.

where the step response values $T_1^{\text{step}}(0, t - t_k)$ are calculated through inversion of equation 36. This calculation is illustrated in figure 13.b.

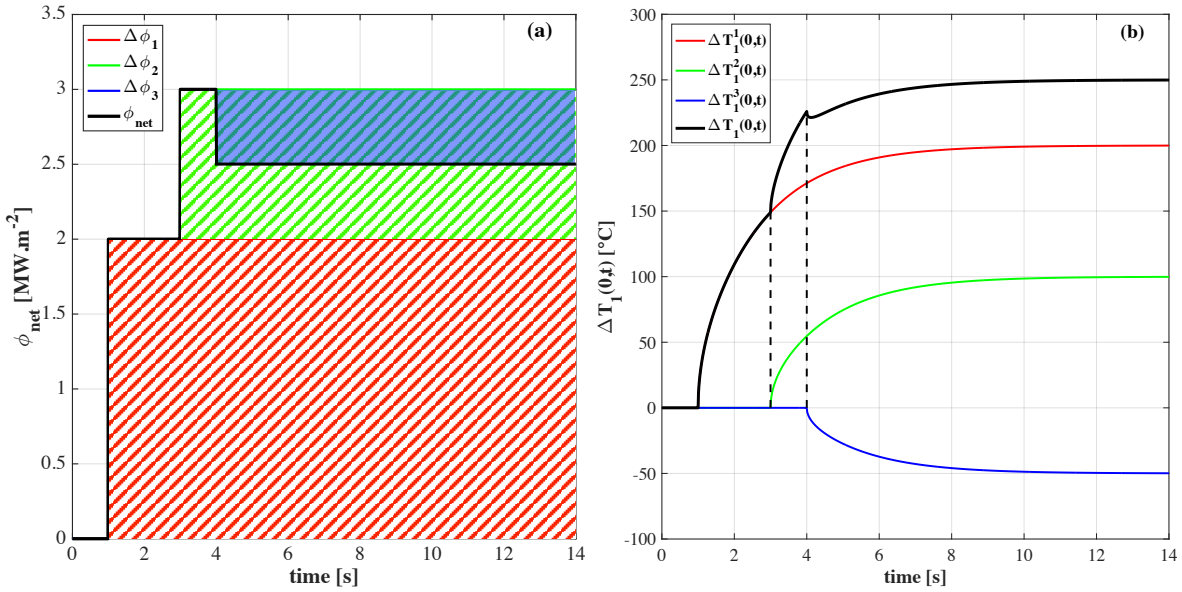

Figure 13: (a) Time evolution of the net heat flux density ϕ_{net} (black solid line) imposed to a PFC made of three material layers (cf. table 9 for the layer specifications). ϕ_{net} is decomposed in three step changes $\Delta\phi_k$ depicted in colored areas in (a). The corresponding temperature variations $\Delta T_1^k(0,t)$ are displayed with the same colors for an actively-cooled PFC in (b). The overall temperature variation at the PFC surface $\Delta T_1(0,t)$ (black solid lines) is the sum of these three temperature variations.

Appendix C: PFC step response calculation through the quadrupole method.

This appendix focuses on the calculation of the PFC step response $T_i^{\text{step}}(s, x, t - t_k(s))$ in the general equation of WE-temp 4. For the sake of clarity, the s coordinate will be omitted in the following derivation as it only refers to the considered PFC. To calculate it, the auxiliary system 2 needs to be solved.

First the heat equation in one given material layer i, equation 2a, is solved. To simplify the calculation, the following change of coordinate $X_i = x - x_{i-1}$, which depend on the considered material layer, is used:

$$\rho_i c_{p_i} \frac{\partial T_i^{\text{step}}(X_i, t)}{\partial t} = \lambda_i \frac{\partial^2 T_i^{\text{step}}}{\partial {X_i}^2} \tag{17}$$

One can now apply the Laplace transform to that equation:

$$\begin{aligned}\frac{\partial^2 \theta_i^{\text{step}}}{\partial {X_i}^2}(X_i,p) &= \frac{1}{a_i}\left(p\theta_i^{\text{step}}(X_i,p) - \cancel{T_i^{\text{step}}(X_i,0)}\right)\\ \frac{\partial^2 \theta_i^{\text{step}}}{\partial {X_i}^2}(X_i,p) &= \frac{p}{a_i}\theta_i^{\text{step}}(X_i,p)\end{aligned} \tag{18}$$

where θ_i^{step} is the Laplace transform of T_i^{step} and $a_i = \lambda_i/(\rho_i c_{p_i})$ is the material heat diffusivity. The initial condition 2e has also been accounted. Such differential equation has the following solution:

$$\theta_i^{\text{step}}(X_i,p) = k_1(p)\cosh(\alpha_i X_i) + k_2(p)\sinh(\alpha_i X_i) \tag{19}$$

where $\alpha_i = \sqrt{p/a_i}$ and k_1 and k_2 are two functions of p. Now one will remember the Fourier law of heat conduction, which relates the mean heat flux density in the material ϕ_i with the temperature:

$$\phi_i(X_i,t) = -\lambda_i \frac{\partial T_i^{\text{step}}}{\partial X_i}(X_i,p) \tag{20}$$

The Laplace transform can also be applied to that law:

$$\Phi_i(X_i,p) = -\lambda_i \frac{\partial \theta_i^{\text{step}}}{\partial X_i} = -\lambda_i\alpha_i k_1(p)\sinh(\alpha_i X_i) - \lambda_i\alpha_i k_2(p)\cosh(\alpha_i X_i) \tag{21}$$

where Φ_i is the Laplace transform of ϕ_i. Both equations 19 and 21 can be written at $X_i = 0$ ($x = x_{i-1}$) and $X_i = e_i$ ($x = x_i$):

$$\begin{cases}\theta_i^{\text{step}}(0,p) = k_1(p)\\ \Phi_i(0,p) = -\lambda_i\alpha_i k_2(p)\\ \theta_i^{\text{step}}(e_i,p) = k_1(p)\cosh(\alpha_i e_i) + k_2(p)\sinh(\alpha_i e_i)\\ \Phi_i(e_i,p) = -\lambda_i\alpha_i k_1(p)\sinh(\alpha_i e_i) - \lambda_i\alpha_i k_2(p)\cosh(\alpha_i e_i)\end{cases} \tag{22}$$

After some algebra, one can eliminate k_1 and k_2 to obtain the following expression relating θ_i^{step} and Φ_i at the boundaries of the material layer (at $x = x_{i-1}$ and $x = x_i$):

$$\begin{pmatrix}\theta_i^{\text{step}}(x_{i-1},p)\\ \Phi_i(x_{i-1},p)\end{pmatrix} = \underbrace{\begin{pmatrix}\cosh(\alpha_i e_i) & \frac{1}{\lambda_i\alpha_i}\sinh(\alpha_i e_i)\\ \lambda_i\alpha_i\sinh(\alpha_i e_i) & \cosh(\alpha_i e_i)\end{pmatrix}}_{M_{mat,i}} \begin{pmatrix}\theta_i^{\text{step}}(x_i,p)\\ \Phi_i(x_i,p)\end{pmatrix} \tag{23}$$

$M_{mat,i}$ is called the quadrupole matrix of the material layer [15].

The same method can be used to treat the interface boundary condition between two adjacent layers (equation 2c). Applying Laplace transform, this equation becomes:

$$\begin{cases}\theta_i^{\text{step}}(x_i,p) = \theta_{i+1}^{\text{step}}(x_i,p) + R_{c_i}\Phi_{i+1}(x_i,p)\\ \Phi_i(x_i,p) = \Phi_{i+1}(x_i,p)\end{cases} \tag{24}$$

which can be written in the following matrix form:

$$\begin{pmatrix}\theta_i^{\text{step}}(x_i,p)\\ \Phi_i(x_i,p)\end{pmatrix} = \underbrace{\begin{pmatrix}1 & R_{c_i}\\ 0 & 1\end{pmatrix}}_{M_{interf,i}} \begin{pmatrix}\theta_{i+1}^{\text{step}}(x_i,p)\\ \Phi_{i+1}(x_i,p)\end{pmatrix} \tag{25}$$

$M_{interf,i}$ is the quadrupole matrix of the interface [15].

Now the N successive material layers of the PFC will be addressed. First the equation 25 can be inserted in equation 23:

$$\begin{aligned}\begin{pmatrix}\theta_i^{\text{step}}(x_{i-1},p)\\ \Phi_i(x_{i-1},p)\end{pmatrix} &= M_{mat,i}\ M_{interf,i}\ \begin{pmatrix}\theta_{i+1}^{\text{step}}(x_i,p)\\ \Phi_{i+1}(x_i,p)\end{pmatrix}\\ \begin{pmatrix}\theta_i^{\text{step}}(x_{i-1},p)\\ \Phi_i(x_{i-1},p)\end{pmatrix} &= \qquad M_{lay,i} \qquad \begin{pmatrix}\theta_{i+1}^{\text{step}}(x_i,p)\\ \Phi_{i+1}(x_i,p)\end{pmatrix}\end{aligned} \tag{26}$$

$M_{lay,i}$ is the generalised quadrupole matrix of a given material layer:

$$M_{lay,i}(p) = \begin{pmatrix}\cosh(\alpha_i e_i) & \dfrac{1}{\lambda_i\alpha_i}\sinh(\alpha_i e_i) + R_{c_i}\cosh(\alpha_i e_i)\\ \lambda_i\alpha_i\sinh(\alpha_i e_i) & \cosh(\alpha_i e_i) + R_{c_i}\lambda_i\alpha_i\sinh(\alpha_i e_i)\end{pmatrix},\ \alpha_i = \sqrt{\frac{p}{a_i}} \tag{27}$$

One can note that if $R_{c_i} = 0$, $M_{lay,i}$ is equivalent to $M_{mat,i}$. Therefore, if one sets $R_{c_N} = 0$, an expression between θ_i^{step} and Φ_i at the boundaries of the PFC (at $x = 0$ and $x = L_x$) is obtained through matrix multiplication of the N matrices $M_{lay,i}$:

$$\begin{pmatrix}\theta_1^{\text{step}}(0,p)\\ \Phi_1(0,p)\end{pmatrix} = M_{lay,1}\ M_{lay,2}\ ...\ M_{lay,i}\ ...\ M_{lay,N-1}\ M_{lay,N}\begin{pmatrix}\theta_N^{\text{step}}(L_x,p)\\ \Phi_N(L_x,p)\end{pmatrix} \tag{28}$$

Equation 28 is a general expression stating the heat transfer through the whole PFC. It does not depend on the type of heat exchange with the surrounding. To do so, one needs to address the B.C. at the top and rear surfaces of the PFC. First, to address the rear B.C (at $x = L_x$), equation 2d must be detailed. If one notes ϕ_{cool} the heat flux density evacuated in the cooling system, this equations becomes:

$$\phi_N(L_x,t) = \phi_{cool}(t) = hT_N^{\text{step}}(L_x,t) \tag{29}$$

By applying Laplace transform and considering Φ_{cool} as the Laplace transform of ϕ_{cool}, equation 29 becomes:

$$\begin{cases}\theta_N^{\text{step}}(L_x,p) = \dfrac{1}{h}\Phi_{cool}(p)\\ \Phi_N(L_x,p) = \Phi_{cool}(p)\end{cases} \tag{30}$$

which can be written in the following matrix form:

$$\begin{pmatrix}\theta_N^{\text{step}}(L_x,p)\\ \Phi_N(L_x,p)\end{pmatrix} = \underbrace{\begin{pmatrix}1 & \dfrac{1}{h}\\ 0 & 1\end{pmatrix}}_{M_{cool}}\begin{pmatrix}0\\ \Phi_{cool}(p)\end{pmatrix} \tag{31}$$

where M_{cool} is the quadrupole matrix of convective B.C. [15]. One can note that M_{cool} is equivalent to $M_{interf,N}$ by setting $R_{c_N} = 1/h$. Therefore a quadrupole matrix of the whole PFC with N layers can be defined:

$$M_{PFC}^N(p) = \begin{pmatrix}A_{PFC}^N(p) & B_{PFC}^N(p)\\ C_{PFC}^N(p) & D_{PFC}^N(p)\end{pmatrix} = \overset{\curvearrowright N}{\prod_{i=1}} M_{lay,i}, R_{c_N} = \frac{1}{h} \tag{32}$$

M_{PFC}^N links the Laplace temperature and heat flux density at the top surface of the PFC with the Laplace temperature and heat flux density of the cooling system. By considering equations 28, 32 and 31, this yields to:

$$\begin{pmatrix}\theta_1^{\text{step}}(0,p)\\ \Phi_1(0,p)\end{pmatrix} = M_{PFC}^N\begin{pmatrix}0\\ \Phi_{cool}(p)\end{pmatrix} = \begin{pmatrix}A_{PFC}^N(p) & B_{PFC}^N(p)\\ C_{PFC}^N(p) & D_{PFC}^N(p)\end{pmatrix}\begin{pmatrix}0\\ \Phi_{cool}(p)\end{pmatrix} \tag{33}$$

By developing equation 33 and eliminating $\Phi_{cool}(p)$, one also obtains a direct relation between the Laplace temperature and heat flux density at the PFC top surface:

$$\theta_1^{\text{step}}(0,p) = \frac{B^N_{PFC}(p)}{D^N_{PFC}(p)}\Phi_1(0,p) \tag{34}$$

Eventually, $\Phi_1(0,p)$ can be obtained from the B.C. at the PFC top surface (equation 2b) and Laplace transform tables [14]:

$$\Phi_1(0,p) = \frac{1}{p} \tag{35}$$

which can be substituted in equation 34:

$$\theta_1^{\text{step}}(0,p) = \frac{1}{p}\frac{B^N_{PFC}(p)}{D^N_{PFC}(p)} \tag{36}$$

Therefore, to obtain the temperature at the PFC surface, the values of the step response at the PFC top surface in the general equation of WE-temp (equations 4), $T_1^{\text{step}}(s, 0, t - t_k(s))$, can be calculated by inverting equation 36 using the inversion formula 10. This integral cannot be calculated analytically but can be estimated numerically using an appropriate algorithm. In WE-temp, such inversion is done using the De Hoog's algorithm [17].

The previous analytical development was focused on the calculation of the surface temperature. To obtain the temperature profile in the first material layer (the layer where the temperature is needed for MHIMS), one only has to consider a first material layer with a thickness $e'_1(x) = e_1 - x$. In that case, the quadrupole matrix of the first material layer is:

$$\begin{aligned}&\underline{\text{for } 0 \leqslant x \leqslant e_1\text{:}}\\ &M'_{lay,1}(x,p) = \begin{pmatrix} \cosh(\alpha_1 e'_1(x)) & \frac{1}{\lambda_1\alpha_1}\sinh(\alpha_1 e'_1(x)) + R_{c_1}\cosh(\alpha_1 e'_1(x)) \\ \lambda_1\alpha_1\sinh(e'_1(x)) & \cosh(\alpha_1 e'_1(x)) + R_{c_1}\lambda_1\alpha_1\sinh(\alpha_1 e'_1(x)) \end{pmatrix}\end{aligned} \tag{37}$$

and a quadrupole matrix of the whole PFC can be defined:

$$\begin{aligned}&\underline{\text{for } 0 \leqslant x \leqslant e_1\text{:}}\\ &M^N_{PFC,1}(x,p) = M'_{lay,1}(x,p) + \overset{\curvearrowleft}{\prod_{i=2}^{N}} M_{lay,i}\ ,\ R_{c_N} = \frac{1}{h}\\ &M^N_{PFC,1}(x,p) = \begin{pmatrix} A^N_{PFC,1}(x,p) & B^N_{PFC,1}(x,p) \\ C^N_{PFC,1}(x,p) & D^N_{PFC,1}(x,p) \end{pmatrix}\end{aligned} \tag{38}$$

One can note that this quadrupole matrix is equivalent to the one of the full PFC, M^N_{PFC}, when x is set to 0.

Now the Laplace temperature at a depth x, $\theta_1^{\text{step}}(x,p)$, will be obtained by analogy with the analytical study for the Laplace surface temperature $\theta_1^{\text{step}}(0,p)$. $M^N_{PFC,1}(x,p)$ links the Laplace temperature and heat flux density at the depth x with the ones of the cooling system:

$$\begin{aligned}\begin{pmatrix} \theta_1^{\text{step}}(x,p) \\ \Phi_1(x,p) \end{pmatrix} &= M^N_{PFC,1}(x,p) \begin{pmatrix} 0 \\ \Phi_{cool}(p) \end{pmatrix}\\ \begin{pmatrix} \theta_1^{\text{step}}(x,p) \\ \Phi_1(x,p) \end{pmatrix} &= \begin{pmatrix} A^N_{PFC,1}(x,p) & B^N_{PFC,1}(x,p) \\ D^N_{PFC,1}(x,p) & D^N_{PFC,1}(x,p) \end{pmatrix} \begin{pmatrix} 0 \\ \Phi_{cool}(p) \end{pmatrix}\end{aligned} \tag{39}$$

By developing equation 39 and eliminating $\Phi_{cool}(p)$ using equation 33, one also obtains a direct relation between $\theta_1^{\text{step}}(x,p)$ and the Laplace heat flux density at the PFC top surface $\Phi_1(0,p)$:

$$\theta_1^{\text{step}}(x,p) = \frac{B^N_{PFC,1}(x,p)}{D^N_{PFC}(p)}\Phi_1(0,p) \text{ for actively-cooled PFCs} \tag{40}$$

One can substitute the expression of $\Phi_1(0,p)$ (equation 35) in equation 40 to obtain the general expression for $\theta_1^{\text{step}}(x,p)$:

$$\underline{\text{for } 0 \leqslant x \leqslant e_1\text{:}}\ \theta_1^{\text{step}}(x,p) = \frac{1}{p}\frac{B_{PFC,1}^N(x,p)}{D_{PFC}^N(p)} \tag{41}$$

Again, to obtain the temperature at a depth x, the values of the step response at a depth x in the general equation of WE-temp (equations 4), $T_1^{\text{step}}(s,x,t-t_k(s))$, are calculated by inverting numerically equation 41 using the inversion formula 10. As in the case of the surface temperature, theses inversions are done using the De Hoog's algorithm [17].

Appendix D: Thickness of PFC materials and initial PFC temperature considered for the DWE simulation.

The JET PFCs have complex geometries. In WE-temp, they are modelled assuming a simpler slab geometry. To recover thermal characteristics of this type of PFCs, we can adjust the thickness of the materials. An equivalent slab geometry of the PFC is set by defining an effective thickness for the main material layer (Be for first-wall PFCs, CFC for inner and outer divertor tiles and W for the tile 5 stacks). This effective thickness, e_{eff}, is calculated as follows, $e_{\text{eff}} = V_{\text{tile}}/A_{\text{wetted}}$, where V_{tile} is the tile volume and A_{wetted} is the wetted surface of the tile [13]. For each PFC, V_{tile} and A_{wetted} are taken from Computer Assisted Drawings. The values of e_{eff} range from 2 to 5 cm. This procedure enables the different zones where the heat flux density is uniform to experience a good inter-pulse temperature increase plasma after plasma (provided that the energy accumulated by the tile, given by the SolEdge-EIRENE simulation, is correct) [13]. In tile 3 and tile 5 Stack C hosting the strike-points, the heat flux density is peaked and reaches a high value. To avoid inter-pulse over-heating, their effective thickness has been increased to 20 cm for the CFC layer and for the W layer respectively [13].
Moreover, the initial temperature of the different PFCs, $T_0(s)$ in equation 4, is taken at the start of the day of operation from thermocouple measurements for the divertor region, leading to temperatures ranging between 50 and 70 °C. Such measurements are not available for the first-wall PFCs. They are considered at the minimum working temperature of the JET-ILW first-wall, i.e. 200 °C. Eventually, the value of the material thermal properties (thermal conductivity, specific heat and material density) have been considered at the closest temperature to the initial temperature of the different regions of the vacuum vessel [31].

Appendix E: Materials set-up for the DWE simulation.

The free-parameters of the MHIMS equations considered for the DWE simulation of D plasma discharges in a full-W JET tokamak are summed up in table 10.
A Dirichlet boundary condition at the rear surface is considered (cf. equation 5d) as the simulated depth of the material (0.1 mm) is high enough to ensure that no mobile deuterium reaches this surface in the time period of the simulation.
Regarding the W traps that can accommodate D, the detrapping energies and trap density profiles defined by Hodille et al. [20] are used. They were obtained through fitting with the Reaction-Diffusion code MHIMS of the experiment of D implantation in W followed by thermal desorption spectrometry made by Ogorodnikova et al. [26]. Three traps are considered: two intrinsic traps and one trap induced by plasma irradiation. Their profiles and respective detrapping energies are displayed in figure 14. The intrinsic traps 1 and 2 have a flat depth profile and were respectively attributed to dislocations and/or iron impurities and to grain boundaries. The plasma-induced trap 3 presents two damaged zones: a highly damaged zone in the implantation zone, attributed to thermodynamic formation of vacancies [35] and often referred to as *super-saturated layer*, and a damaged zone extending in the depth of the material, which could be attributed to vacancies filled with light impurities originating from the

DIFFUSION		
Parameter	Value	From
D_0	$1.9 \times 10^{-7}/\sqrt{A}$ m^2.s^{-1}	Density Functional Theory [32]
E_{diff}	0.2 eV	Density Functional Theory [32]
$A = m_{\text{D}}/m_{\text{H}}$	2	—
TRAPPING		
Parameter	Value	From
$\nu^0_{\text{t},i}$	${D_0}/{\lambda_{\text{W}}}^2$	—
λ_{W}	111.7 pm	Experiment [33] and Density Functional Theory [32]
$E_{\text{t},i}$	0.2 eV	—
n_{IS}	$6\rho_{\text{W}}$	Density Functional Theory [32]
ρ_{W}	6.3382×10^{28} m^{-3}	[34]
DETRAPPING		
Parameter	Value	From
$\nu^0_{\text{dt},i}$	10^{13} s^{-1}	—

Table 10: Parameters of the Reaction-Diffusion equations considered for the DWE simulation of D plasma discharges in a full-W JET tokamak.

plasma (carbon, oxygen) as suggested by experiments [36, 37]. Two sets of trap distribution were used to model massive W in MHIMS: one in the divertor region and one in the first-wall region (cf. figure 2, from point 2 to point 1 clockwise). The difference between the sets lies in the definition of the plasma-induced trap 3 to account for different plasma-wall interactions in the two regions. For both wall regions, we consider that the damaged implantation zone has reached its saturation value defined by Hodille et al. [18], i.e. 15 at.% of W. However, the extent of this damaged zones differs in the two regions of the wall. In the divertor, it is considered that the implantation zone extends up to 30 nm which corresponds to the maximum implantation range of 1 keV D in W. Such implantation conditions can be found in the divertor during ELM events. For the first-wall region, this damaged region extends up to 20 nm which corresponds to the maximum implantation range of 0.5 keV D in W. One can expect that, during H-mode plasma, charge exchange neutrals with such energy escape from the pedestal region and hit the first-wall. Regarding the bulk part, its depth extent is linked to diffusion of impurities in the depth of the material. The higher the W working temperature is, the deeper the impurities diffuse and the deeper trap 3 is created [20]. In this simulation, it was assumed that the divertor had experienced a working temperature of 1000 ℃ during plasma operation while the first-wall was maintained at its base temperature of 200 ℃. This difference of working temperature leads to a deeper trap 3 density profile in the divertor than in the first-wall (cf. figure 14). Such traps definition is representative of W that has experienced hours of plasma operation.

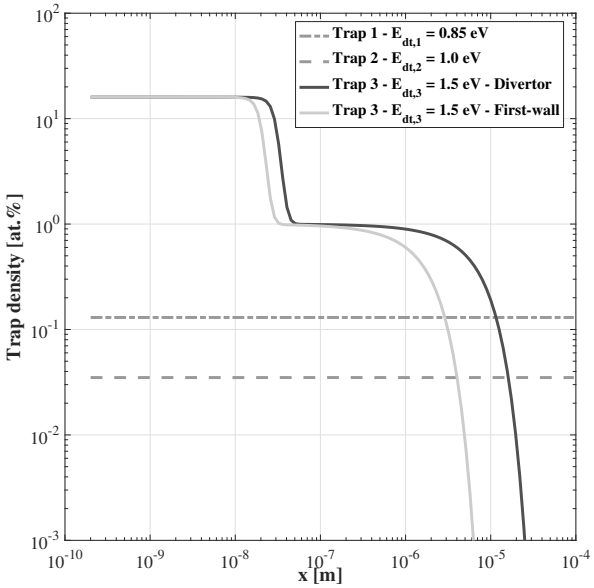

Figure 14: Density profiles of traps and related detrapping energies used in the DWE simulation of D plasma discharges in a full-W JET tokamak. The densities are expressed in atomic fraction of W (%).

References

[1] S. Brezinsek et al. Fuel retention studies with the ITER-Like Wall in JET. Nuclear Fusion, 53(8):083023, 2013.

[2] V. Philipps et al. Dynamic fuel retention and release under ITER like wall conditions in JET. Journal of Nuclear Materials, 438:S1067 – S1071, 2013. Proceedings of the 20th International Conference on Plasma-Surface Interactions in Controlled Fusion Devices.

[3] C. Grisolia. Plasma wall interaction during long pulse operation in tore supra. Journal of Nuclear Materials, 266-269:146 – 152, 1999.

[4] T Nakano, N Asakura, H Takenaga, H Kubo, Y Miura, K Shimizu, S Konoshima, K Masaki, S Higashijima, and the JT-60Team. Impact of wall saturation on particle control in long and high-power-heated discharges in JT-60u. Nuclear Fusion, 46(5):626–634, apr 2006.

[5] T. Loarer et al. Gas balance and fuel retention in fusion devices. Nuclear Fusion, 47(9):1112–1120, aug 2007.

[6] H. Bufferand et al. Numerical modelling for divertor design of the WEST device with a focus on plasma–wall interactions. Nuclear Fusion, 55(5):053025, apr 2015.

[7] J. Denis et al. Dynamic modelling of local fuel inventory and desorption in the whole tokamak vacuum vessel for auto-consistent plasma-wall interaction simulations. Nuclear Materials and Energy, 19:550 – 557, 2019.

[8] H. Kawamura et al. Retention of deuterium implanted in hot-pressed beryllium. Journal of Nuclear Materials, 176-177:661 – 665, 1990.

[9] W. R. Wampler. Retention and thermal release of deuterium implanted in beryllium. Journal of Nuclear Materials, 123(1):1598 – 1602, 1984.

[10] A. V. Markin et al. Thermal desorption of deuterium implanted into beryllium. Journal of Nuclear Materials, 233-237:865 – 869, 1996.

[11] A. A. Haasz and J. W. Davis. Deuterium retention in beryllium, molybdenum and tungsten at high fluences. Journal of Nuclear Materials, 241-243:1076 – 1081, 1997.

[12] M. Reinelt et al. Retention mechanisms and binding states of deuterium implanted into beryllium. New Journal of Physics, 11(4):043023, apr 2009.

[13] Julien Denis. Dynamic modelling of local fuel desorption and retention in the wall of nuclear fusion reactors for auto-consistent plasma-wall interaction simulations. Theses, Aix-Marseille Université (AMU), December 2019.

[14] N. Ozisik. Heat Conduction - Second Edition. 1980.

[15] D. Maillet et al. Thermal Quadrupoles: Solving the Heat Equation through Integral Transforms. 2000.

[16] J. Denis et al. Wall surface temperature calculation in the soledge2d-eirene transport code. Physica Scripta, 2016(T167):014073, 2016.

[17] F. R. de Hoog et al. An improved method for numerical inversion of laplace transforms. SIAM Journal on Scientific and Statistical Computing, 3(3):357–366, 1982.

[18] E. A. Hodille et al. Macroscopic rate equation modeling of trapping/detrapping of hydrogen isotopes in tungsten materials. Journal of Nuclear Materials, 467:424 – 431, 2015.

[19] A. McNabb and P. K. Foster. A new analysis of the diffusion of hydrogen in iron and ferritic steels. Transactions of the Metallurgical Society of AIME, 227(3):618, 1963.

[20] E. A. Hodille. Study and modeling of the deuterium trapping in ITER relevant materials. Theses, UNIVERSITE D'AIX-MARSEILLE, November 2016.

[21] J. F. Ziegler, M. D. Ziegler, and J. P. Biersack. SRIM – The stopping and range of ions in matter (2010). Nuclear Instruments and Methods in Physics Research Section B: Beam Interactions with Materials and Atoms, 268(11):1818 – 1823, 2010. 19th International Conference on Ion Beam Analysis.

[22] A. Widdowson et al. Overview of fuel inventory in jet with the iter-like wall. Nuclear Fusion, 57(8):086045, 2017.

[23] D. Matveev et al. Reaction-diffusion modeling of hydrogen transport and surface effects in application to single-crystalline Be. Nuclear Instruments and Methods in Physics Research Section B: Beam Interactions with Materials and Atoms, 430:23 – 30, 2018.

[24] Anže Založnik, Matthew J. Baldwin, Michael J. Simmonds, and Russell P. Doerner. Modeling the sharp deuterium release from beryllium co-deposits. Nuclear Fusion, 59(12):126027, oct 2019.

[25] R. A. Anderl et al. Hydrogen isotope retention in beryllium for tokamak plasma-facing applications. Journal of Nuclear Materials, 273(1):1 – 26, 1999.

[26] O. V. Ogorodnikova et al. Deuterium retention in tungsten in dependence of the surface conditions. Journal of Nuclear Materials, 313-316:469 – 477, 2003. Plasma-Surface Interactions in Controlled Fusion Devices 15.

[27] J. Denis, E.A. Hodille, Y. Marandet, and Y. Ferro. Analytical model of hydrogen inventory saturation in the subsurface of the wall material and comparison to reaction-diffusion simulations. Journal of Nuclear Materials, 570:153972, 2022.

[28] H. Atsumi, Y. Takemura, T. Miyabe, T. Konishi, T. Tanabe, and T. Shikama. Desorption of hydrogen trapped in carbon and graphite. Journal of Nuclear Materials, 442(1, Supplement 1):S746–S750, 2013. FIFTEENTH INTERNATIONAL CONFERENCE ON FUSION REACTOR MATERIALS.

[29] E.A. Hodille, L.B. Begrambekov, J.Y. Pascal, O. Saidi, J.M. Layet, B. Pégourié, and C. Grisolia. Hydrogen trapping in carbon film: From laboratories studies to tokamak applications. International Journal of Hydrogen Energy, 39(35):20054–20061, 2014.

[30] A. Widdowson et al. Overview of the jet iter-like wall divertor. Nuclear Materials and Energy, 12:499 – 505, 2017. Proceedings of the 22nd International Conference on Plasma Surface Interactions 2016, 22nd PSI.

[31] V. Barabash. Summary of material properties for structural analysis of the ITER internal components. ITER Organization.

[32] N. Fernandez et al. Hydrogen diffusion and vacancies formation in tungsten: Density Functional Theory calculations and statistical models. Acta Materialia, 94:307 – 318, 2015.

[33] V. T. Deshpande and R. Pawar. X-Ray determination of the thermal expansion of tungsten. Current Science, 31(12):497–499, 1962.

[34] H. Pastor. Propriétés du tungstène et de ses alliages. Techniques de l'ingénieur Métaux et alliages non ferreux, base documentaire : TIB357DUO.(ref. article : m570), 1985. fre.

[35] E. A. Hodille, N. Fernandez, Z. A. Piazza, M. Ajmalghan, and Y. Ferro. Hydrogen supersaturated layers in H/D plasma-loaded tungsten: A global model based on thermodynamics, kinetics and density functional theory data. Phys. Rev. Materials, 2:093802, Sep 2018.

[36] M. Poon et al. Flux dependence of deuterium retention in single crystal tungsten. Journal of Nuclear Materials, 307-311:723 – 728, 2002.

[37] M. Poon et al. Effects of background gas impurities during d+ irradiation on d trapping in single crystal tungsten. Journal of Nuclear Materials, 337-339:629 – 633, 2005. PSI-16.